WILEY | Hindawi

Research Article

The Role of Coal Mechanical Characteristics on Reservoir Permeability Evolution and Its Effects on CO$_2$ Sequestration and Enhanced Coalbed Methane Recovery

Hao Han [ID],[1,2] **Shun Liang** [ID],[1,2,3] **Yaowu Liang** [ID],[1] **Xuehai Fu** [ID],[3] **Junqiang Kang** [ID],[3] **Liqiang Yu** [ID],[1] **and Chuanjin Tang** [ID][1]

[1]*State Key Laboratory of Coal Resource and Mine Safety, School of Mines, China University of Mining and Technology, Xuzhou, Jiangsu 221008, China*
[2]*College of Mining Engineering, Liaoning Technical University, Fuxin, Liaoning 123000, China*
[3]*Key Laboratory of CBM Resources and Reservoir Formation Process, Ministry of Education, China University of Mining and Technology, Xuzhou, Jiangsu 221008, China*

Correspondence should be addressed to Shun Liang; 5756@cumt.edu.cn

Elastic modulus is an important parameter affecting the permeability change in the process of coalbed methane (CBM)/enhanced coalbed methane (ECBM) production, which will change with the variable gas content. Much research focuses on the constant value of elastic modulus; however, variable stiffness of coal during CO$_2$ injection has been considered in this work. The coupled thermo-hydro-mechanical (THM) model is established and then validated by primary production data, as well as being applied in the prediction of CO$_2$/N$_2$-ECBM recovery. The results show that the harder coal seam is beneficial to primary production, while the softer coal seam results in greater CO$_2$/N$_2$-ECBM recovery and CO$_2$ sequestration. N$_2$ and CO$_2$ mixture injection could be applied to balance early N$_2$ breakthrough and pronounced matrix swelling induced by CO$_2$ adsorption, and to prolong the process of effective CH$_4$ recovery. Besides, reduction in stiffness of coal seam during CO$_2$ injection would moderate the significant permeability loss induced by matrix swelling. With the increase of the weakening degree of coal seam stiffness, CO$_2$ cumulative storage also shows an increasing trend. Neglecting the weakening effect of CO$_2$ adsorption on coal seam stiffness could underestimate the injection capacity of CO$_2$. Injection of hot CO$_2$ could improve the permeability around injection well and then enhance CO$_2$ cumulative storage and CBM recovery. Furthermore, compared with ECBM production, injection temperature is more favorable for CO$_2$ storage, especially within hard coal seams. Care should be considered that significant permeability change is induced by mechanical characteristics alterations in deep burial coal seams in further study, especially for CO$_2$-ECBM projects.

1. Introduction

Coal seams are typified as dual-porosity systems consisting of micropores in a matrix and two sets of cleats. Coal matrix contains more than 95% adsorption of methane (CH$_4$) with the cleat systems providing an effective flow path for both water and gas [1, 2]. Primary coalbed methane (CBM) recovery begins with the dewatering to reduce reservoir pressure and increase gas effective permeability [3, 4]. However, it is generally acknowledged that less than 50% of methane *in situ*

could be extracted by traditional method due to higher adsorption capacity of coal, which is not efficient or economical [5, 6]. Therefore, CBM production enhancement techniques have been conducted in some field trials to stimulate the methane recovery rate in recent twenty years.

The ECBM recovery technique is possible using two methods, involving injection of N$_2$ (N$_2$-ECBM) and CO$_2$ (CO$_2$-ECBM) [7–9]. Both the two injectants could reduce the CH$_4$ partial pressure in the cleats, then promote CH$_4$ desorption from the coal matrix to achieve the new partial

pressure equilibrium [10, 11]. Besides, CO_2 can also displace CH_4 from coal seams due to a greater affinity to coal [12]. N_2 is weakly adsorbed than CH_4 in coal, which results in a better sweeping efficiency, and thus is mainly maintained in the free gas phase [13]. This process is also referred to as CH_4 stripping. As an added benefit, injecting N_2/CO_2 can sustain the positive effects of a higher total reservoir pressure on permeability and accelerate the gas flow rate by adding the additional driving force [14]. For the project of CO_2-ECBM, besides the effect of ECBM recovery, accompanying geological storage of CO_2 can be viewed as a potential means to mitigate greenhouse gas emission [15]. Since the first field trial of CO_2-ECBM in the Allison unit, San Jan Basin in 1995, a number of field pilots were conducted in Canada, Japan, Europe, and China, subsequently [16]. Meanwhile, N_2, which is cheap and abundant, has been introduced to overcome pronounced permeability loss during CO_2 injection in several field applications, including Yubari pilot, Japan and Tiffany unit, San Jun Basin [17].

Coal permeability is an important parameter for primary CBM production or ECBM recovery. There are generally two competing effects on the absolute permeability, i.e., changed effective stress and coal matrix shrinkage/swelling. For primary production, depressurization increases the effective stress and causes a reduction in the permeability due to cleat compression, and then the permeability may tend to rebound due to coal matrix shrinkage [18–20]. However, CO_2 has a great affinity to coal than CH_4 and N_2; thus, significant matrix swelling caused by CO_2 adsorption may result in permeability and well injectivity loss during CO_2 injection [21, 22], which has been one of the technical obstacles suffered in CO_2-ECBM recovery or CO_2 storage. A reduction of over two orders of magnitude in injection well permeability of Allison CO_2-ECBM pilots has been reported [23]. Unlike primary production, where permeability changes due to coal matrix shrinkage may show an important effect at the late production stage, net matrix swelling induces severe permeability loss which can be observed at early or whole stages of CO_2 injection [17]. Furthermore, the dramatic reduction in injectivity and permeability has not been observed in field trials and laboratory tests, where pure N_2 or flue gas was used [11, 24, 25] due to net matrix shrinkage caused by a much lower sorption capacity and strain of N_2.

Coal mechanical properties are important in the design of primary CBM/ECBM recovery and CO_2 sequestration due to the influence of elastic modulus on controlling the stiffness of the cleat systems [26]. Compared with N_2 injection, CO_2 adsorption could not only cause matrix swelling but also pronouncedly reduce the stiffness and strength of coal (9.6%-82.1% for uniaxial compression; 12.16%-20% for triaxial compression), and consequently the permeability changes. To date, many field and laboratory experiments have been conducted on investigating the mechanical behavior of CO_2 interaction with coal [27–31]. The consequent mechanical properties alteration depends on its geoenvironment and coal seam characteristics, including confining stress, CO_2 adsorption pressure, CO_2 phase state, CO_2 saturation time, coal rank, cleat density and orientation, and moisture [26]. For instance, CO_2-induced coal strength and stiffness reduction is comparatively less under higher *in situ* stress state [27, 32, 33], due to the decreased CO_2 adsorption and potentially hindered by matrix swelling. With the increase of adsorption pressure, the mechanical degradation caused by CO_2 adsorption is also gradually elevated [33]. Similarly, the CO_2 phase changes into supercritical state would create a significant strength and stiffness reduction since the higher adsorption capacity and polymerization capacity than that in the subcritical state. Note that the reduction of the mechanical strength and the stiffness (elastic modulus) with the CO_2 saturation pressure could be mathematically described by Langmuir-type curves [26, 34]. Moreover, almost overall previous investigations imply that mechanical degradation largely occurs during the initial exposure to CO_2, while the additional CO_2 exposure only reduces the strength parameters slightly. There are a number of factors that contribute to the comprehensive coal mechanical properties alteration, including changed surface energy, plasticization and swelling effects [27, 35], microcracks induced by differential swelling/shrinkage strain [36], and dissolution of minerals due to chemical interactions [26, 37, 38]. Therefore, there might be the third effect that dominates the evolution of permeability besides effective stress and matrix strain—the stiffness of coal decreases, which would enhance the positive effect of the reduction in effective stress and moderate the significant matrix swelling (the influence may be more pronounced under supercritical CO_2 state) during CO_2 injection. The ultimate performance of reservoir permeability should be the result of coupling and competition of the above three aspects.

Understanding the mechanism of coal mechanical properties on coupled processes is key to evaluate the efficiency of CO_2 sequestration and ECBM recovery. Especially, the anomalous phenomenon, which shows enhanced injectivity in a few CO_2-ECBM field trials [39] and CO_2 permeability rebound in laboratory experiments [40], might be potentially attributed to the CO_2-coal interaction. In this study, we firstly address these key issues of a lack of investigations—involving geomechanical response on the effect of CO_2/N2-ECBM recovery through developing coupled thermo-hydro-mechanical (THM) modeling. Then, the modeling is employed to inversing the reservoir permeability evolution, CH_4 production rate/cumulative production, CO_2 storage rate/cumulative storage, and CO_2/N_2 breakthrough. Additionally, analysis and discussion are offered to link the modeling results with the field/laboratory observations.

2. Coupled Model for THM

2.1. Conceptual Model and Assumptions. CO_2/N_2-ECBM recovery involve the processes of competitive adsorption induced by a more reactive gas (CO_2), inert gas stripping (N_2), gas diffusion between matrix and cleats, gas and water two-phase flow in cleats, and heat transfer, together with coal deformation induced by the change in effective stress. The general processes of complex interactions are manifest in the response to THM coupling in the coal seams and schematically shown in Figure 1. A set of field-governing equations are defined that govern coal deformation and the
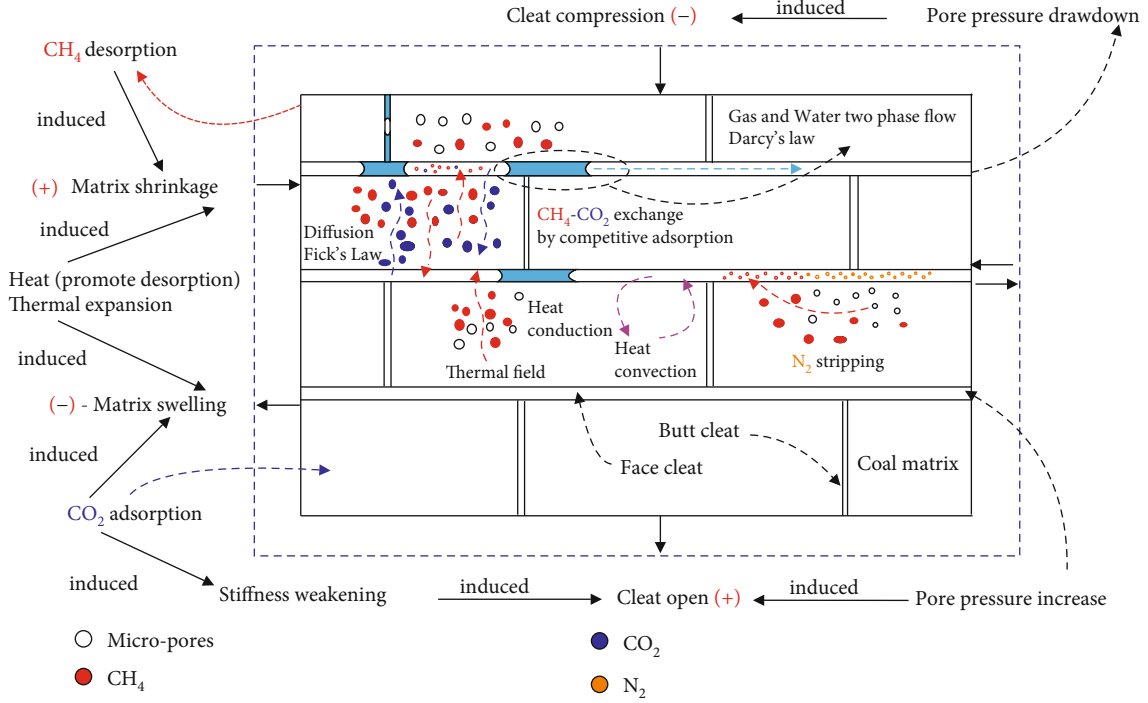
FIGURE 1: Mass transport processes for binary gas (CO_2/N_2, CH_4) and water during CBM, CO_2/N_2-ECBM recovery, and injection heat.

transport of fluids and heat. The assumptions are adopted for the model: (a) The coal seam is a single-permeability poroelastic material; (b) water migrates only in the cleats, and the binary gas (CH_4, N_2/CO_2) exists and migrates in both the matrix micropores and cleats; (c) competitive adsorption between CH_4 and CO_2 in the matrix satisfies the modified the extend Langmuir equation; and (d) fluid flows within the cleats satisfy Darcy's law, and the gas diffusion between the matrix and fractures follows Fick's Law.

2.2. Governing Equations

2.2.1. Governing Equation of the Hydraulic Field. The representative elemental volume (REV) includes fractures and coal matrix with the equation for the mass balance of the water and gas two-phase flow in the REV defined as

$$\frac{\partial m}{\partial t} + \nabla \bullet \left(\rho_p \boldsymbol{v_p} \right) = Q_s, \quad (1)$$

where ρ_p is the gas or water density, kg/m³; $\boldsymbol{v_p}$ indicates the Darcy velocity of the gas or water phase, m/s; t denotes the time, s; Q_s is a source term, kg m⁻³ s⁻¹; and m indicates the methane or water content, kg/m³.

The binary gas content in the REV comprises both free-phase gas in the fractures (m_{fg}) and adsorbed gas content (V_{sg}) in matrix and is expressed as

$$m_{gi} = m_{fgi} + \rho_c \rho_{gsi} \left(1 - \varphi_f \right) V_{sgi} = \rho_{fgi} \varphi_f S_g + \rho_c \rho_{gsi} \left(1 - \varphi_f \right) V_{sgi}, \quad (2)$$

where ρ_c is the coal density, kg/m³; ρ_{gsi} represents the gas density under standard conditions (the subscript i represents the gas component, $i = 1$ for CH_4 and $i = 2$ for CO_2/N_2); φ_f denotes the fracture porosity; S_g indicates the gas saturation; ρ_{fg} is the free gas density within the fractures, m³/kg; ρ_{mg} represents the free gas density in the matrix micropores, m³/kg; and p_m is the gas pressure in the matrix, Pa. Then, according to the ideal gas law, the gas density can be described as $\rho_{fgi} = M_{gi} p_{fgi}/RT$, where M_{gi} is the molar mass of the gas component i, g/mol; R is the universal gas content, J/(mol·K); and T is the reservoir temperature , K.

The absorbed gas content in per unit coal mass under variable temperature can be improved by the modified Langmuir equation [41–43]:

$$V_{sgi} = \frac{V_{Li} b_i p_{mgi}}{1 + \sum_{i=1}^{2} b_i p_{mgi}} \exp \left(-\frac{c_1}{1 + c_2 p_m} (T - T_{\text{ref}}) \right), \quad (3)$$

where c_1 and c_2 are the thermal coefficients of gas adsorption; V_{Li} is the Langmuir volume constant of gas component i, m³/kg; P_{Li} is the Langmuir pressure constant of gas component i, Pa; $b_i = 1/P_{Li}$; p_{mgi} is the gas pressure of component i in the matrix, Pa; T and T_{ref} are the reservoir temperature under the conditions of current and reference state, respectively, K; and $p_m = p_{mg1} + p_{mg2}$ is the total gas pressure in the matrix, Pa.

Then, the water content in the REV can be expressed as follows:

$$m_w = \rho_w \varphi_f S_w, \tag{4}$$

where ρ_w is water density, kg/m^3, and S_w is water saturation, $S_w + S_g = 1$.

The reservoir pressure is defined as [42]

$$p_f = S_g \left(p_{fg1} + p_{fg2} \right) + S_w p_{fw}, \tag{5}$$

where p_{fg} is gas pressure in the fractures, MPa, and p_{fw} indicates the water pressure in the fractures, Pa.

The relationship between the gas pressure and water pressure can be expressed as [44]

$$p_{cgw} = p_{fg} - p_{fw}, \tag{6}$$

where p_{cgw} is the capillary pressure, Pa.

Buoyancy is not considered for both gas and water, defining Darcy's law for two-phase flow in the fractures as

$$\boldsymbol{v_{gi}} = -\frac{k_{eg}}{\mu_{gi}} \nabla p_{fgi}, \tag{7}$$

$$\boldsymbol{v_w} = -\frac{k_{ew}}{\mu_w} \nabla p_{fw}, \tag{8}$$

where the subscripts g and w refer to the gas and water, respectively; $\boldsymbol{v_{gi}}$ and $\boldsymbol{v_w}$ indicate the Darcy law velocity of the gas component i and water, respectively, m/s; μ_{gi} and μ_w denote the dynamic viscosity; k_{eg} and k_{ew} are the effective permeability of the gas and water, respectively, m^2.

The mass exchange between matrix and fractures are dominated by diffusion, which may be defined as [45, 46]

$$q = -\frac{\partial m_{mg}}{\partial t} = -D\sigma_c \left(\rho_{mgi} - \rho_{fgi} \right) = -D\sigma_c \frac{M_{gi}}{RT} \left(p_{mgi} - p_{fgi} \right), \tag{9}$$

where q is the gas exchange rate between the matrix and the fractures, kg/(m^3·s); σ_c indicates the coal matrix block shape factor, m^{-2}; D is the gas diffusion coefficient, m^2/s; ρ_{mg} indicates the concentration of gas in the matrix blocks, kg/m^3; and we use adsorption time to estimate the effective gas diffusion coefficient in the coal matrix as [47]

$$\tau = \frac{1}{D\sigma_c}, \tag{10}$$

where τ is the sorption time of the coal matrix, which is numerically equivalent to the time for 63.2% of the coal gas to be recovered, s.

Enabling the substitution of Eqs. (3) and (10) into Eq. (9) returns the governing equations of the diffusion field as

$$-\frac{\partial}{\partial t} \left(\rho_c \rho_{gsi} \left(1 - \varphi_f \right) \frac{V_{Li} b_i p_{mgi}}{1 + \sum_{i=1}^{2} b_i p_{mgi}} \exp \left(-\frac{c_1}{1 + c_2 p_m} \left(T - T_{ref} \right) \right) \right)$$
$$= \frac{1}{\tau} \frac{M_{gi}}{RT} \left(p_{mgi} - p_{fgi} \right). \tag{11}$$

Finally, by substituting Eqs. (2), (3), (4), (7), and (8) into Eq. (1), the governing equations of two-phase flow in cleats are obtained as

$$\frac{\partial}{\partial t} \left(\frac{M_{gi}}{RT} P_{fgi} \varphi_f S_g + \rho_c \rho_{gs} \left(1 - \varphi_f \right) \frac{V_L p_{mgi}}{p_{mgi} + P_L} \right)$$
$$= \nabla \bullet \left(\frac{M_{gi}}{RT} P_{fg} \frac{k_{eg}}{\mu_g} \nabla p_{fgi} \right), \tag{12}$$

$$\frac{\partial}{\partial t} \left(\rho_w \varphi_f S_w \right) = \nabla \bullet \left(\rho_w \frac{k_{ew}}{\mu_w} \nabla p_{fw} \right). \tag{13}$$

Combining Eqs. (11), (12), and (13) defines the governing equation of the transport field.

2.2.2. Governing Equation of the Mechanical Field. For a homogeneous, isotropic, and elastic medium, the strain-displacement relationship and the equilibrium equation can be expressed as follows:

$$\varepsilon_{ij} = \frac{1}{2} \left(u_{i,j} + u_{j,i} \right), \tag{14}$$

$$\sigma_{ij,j} + f_i = 0, \tag{15}$$

where ε_{ij} represents the strain tensor ($i, j = 1, 2, 3$); u_i is the displacement within the element; σ_{ij} is the total stress tensor; and σ_{ij}^e is the effective stress tensor, and effective stresses are defined as $\sigma_{ij}^e = \sigma_{ij} - \alpha p_f$.

The constitutive relationship of an isotropic linear poroelastic medium is expressed as [48]

$$\varepsilon_{ij} = \frac{1}{2G} \sigma_{ij} - \left(\frac{1}{6G} - \frac{1}{9K} \right) \sigma_{kk} \delta_{ij} + \frac{\alpha p_f}{3K} \delta_{ij} + \frac{\varepsilon_s}{3} \delta_{ij} + \frac{\varepsilon_T}{3} \delta_{ij}, \tag{16}$$

where $G = E/2(1 + v)$ is the shear modulus, Pa; $K = E/3(1 - 2v)$ represents the bulk modulus of the coal, and K_s represents the bulk modulus of the coal grains, Pa; α is the Biot coefficient and can be expressed as $\alpha = 1 - K/K_s$; E is Young's modulus of the coal seam, Pa; E_s is Young's modulus of the coal grains, Pa; v is Poisson's ratio; δ_{ij} is the Kronecker delta tensor defined as 1 for $i = j$ and 0 for $i \neq j$; f_i denotes the components of the body forces; $\sigma_{kk} = \sigma_{11} + \sigma_{22} + \sigma_{33}$. $\varepsilon_s = \varepsilon_{sg1} + \varepsilon_{sg2}$ is the total volumetric strain of matrix swelling/shrinkage induced by binary gas adsorption/desorption; α_T is the

thermal expansion coefficient, 1/K; and $\varepsilon_T = \alpha_T T$ is the thermal expansion volumetric strain.

By analogy, the extended Langmuir-type equation is then used to define the sorption-induced volumetric strain, which can be expressed as

$$\varepsilon_{sgi} = \frac{\varepsilon_{Li} b_i p_{mgi}}{1 + \sum_{i=1}^{2} b_i p_{mgi}} \exp\left(-\frac{c_1}{1 + c_2 p_m}\left(T - T_{ref}\right)\right), \quad (17)$$

where ε_{Li} is the maximum volumetric strain of gas component i.

The Langmuir-type curve is used to describe the elastic modulus reduction (ΔE), and elastic modulus of CO_2 saturated coal mass can be written as [26, 34]

$$E_{CO2} = E_{int} - \Delta E, \quad (18)$$

$$\Delta E = \frac{\Delta E_{max} p_{CO2}}{P_E + p_{CO2}}, \quad (19)$$

where p_{CO2} is the gas component of CO_2, Pa; ΔE_{max} is the maximum reduction in the elastic modulus, Pa; and P_E is the curve-fitting parameter, Pa.

Combining Eqs. (14), (15), and (16)

$$G u_{i,jj} + \frac{G}{1 - 2v} u_{i,ji} - \alpha p_{f,i} - K\varepsilon_{s,i} - K\varepsilon_{T,i} + f_i = 0 \quad (20)$$

yields a modified Navier-type equation defining deformation.

2.2.3. Governing Equation of the Thermal Field. The energy conservation equation of the skeleton and fluid can be obtained based on the energy conservation law. For the projects of CBM and CO_2/N_2-ECBM recovery, variation of internal energy within REV caused by temperature change is equal to the sum of heat convection of fluids (binary gas and water), heat conduction among the solid and fluid phases, strain energy induced by skeleton deformation, and isosteric heat induced by gas adsorption. The governing equation of the thermal field can be expressed as [49–51]

$$C_c^T \frac{\partial T}{\partial t} - \eta_{eff}\nabla T - \nabla \cdot \left(\lambda_c^T \nabla T\right) + K\alpha_T T \frac{\partial \varepsilon_v}{\partial t} + \sum_{i=1}^{2} q_{sti} \frac{\rho_s \rho_{gsi}}{M_{gi}} \frac{\partial V_{sgi}}{\partial t} = 0, \quad (21)$$

where C_c^T is the effective specific heat capacity of the coal mass, J/(m^3 K); η_{eff} is the effective heat convection coefficient of the fluids, J/(m^2·s); λ_c^T is the effective thermal conductivity, W/(m K); and q_{sti} is the isosteric heat of gas adsorption of component i, kJ/mol.

$$C_c^T = \left(1 - \varphi_f\right)\rho_s C_s + \sum_{i=1}^{2} \varphi_f S_g \rho_{fgi} C_{gi} + \rho_w \varphi_f S_w C_w \quad (22)$$

$$\eta_{eff} = -\sum_{i=1}^{2} \frac{\rho_{fgi} C_{gi} k k_{rg}}{\mu_{gi}} \nabla p_{fgi} - \frac{\rho_w C_w k k_{rw}}{\mu_w} \nabla p_{fw} \quad (23)$$

$$\lambda_c^T = \left(1 - \varphi_f\right)\lambda_s + \varphi_f\left(S_g \lambda_{gi} + S_w \lambda_w\right) \quad (24)$$

where C_s, C_{gi}, C_w are the specific heat capacities of coal skeleton, binary gas, and water, respectively, kJ/(kg·K); $\lambda_s, \lambda_{gi}, \lambda_w$ are the thermal conduction coefficients for the coal skeleton, binary gas, and water, respectively, W/(m·K).

2.2.4. Cross-coupling. The permeability and porosity represent the key cross-coupling parameters linking the multiphysic fields. The cubic law is widely applied to describe the absolute permeability change relative to the porosities as

$$\frac{k}{k_0} = \left(\frac{\varphi}{\varphi_0}\right)^3, \quad (25)$$

where the subscript 0 refers to the initial state and k, φ are the absolute permeability and porosity, respectively.

Based on the constitutive relationship of coal mass (Eq. (16)), the volumetric strain of the REV is expressed as

$$\begin{aligned} \Delta\varepsilon_v &= \Delta\varepsilon_{11} + \Delta\varepsilon_{22} + \Delta\varepsilon_{33} \\ &= \frac{(\Delta\sigma_{11} + \Delta\sigma_{22} + \Delta\sigma_{33})}{3K} + \frac{\alpha\Delta p}{K} + \Delta\varepsilon_s + \Delta\varepsilon_T \\ &= \frac{-(\Delta\sigma^- - \alpha\Delta P)}{K} + \Delta\varepsilon_s + \Delta\varepsilon_T, \end{aligned} \quad (26)$$

where $\sigma^- = -\sigma_{kk}/3$ is the mean compressive stress.

Considering a porous medium containing solid volume of V_s and pore volume of V_P, we assume the bulk volume $V_b = V_P + V_s$, the porosity, and its differential form can be expressed as Eq. (27) and Eq. (28), respectively.

$$\varphi = \frac{V_P}{V_b}, \quad (27)$$

$$d\varphi = d\left(\frac{V_P}{V_b}\right) = \frac{1}{V_b}dV_P - \frac{V_P}{V_b^2}dV_b = -\varphi(d\varepsilon_b - d\varepsilon_P). \quad (28)$$

According to Eq. (4), the volumetric evolution of the porous medium can be described in terms of the volumetric strain of coal mass ($d\varepsilon_b$) and pore space ($d\varepsilon_P$), respectively. The relations are

$$d\varepsilon_b = \frac{\Delta V_b}{V_b} = \frac{-(\Delta\sigma^- - \alpha\Delta P)}{K} + \Delta\varepsilon_s + \Delta\varepsilon_T, \quad (29)$$

$$d\varepsilon_P = \frac{\Delta V_P}{V_P} = \frac{-(\Delta\sigma^- - \beta\Delta P)}{K_p} + \Delta\varepsilon_s + \Delta\varepsilon_T, \quad (30)$$

where $\beta = 1 - K_P/K_s$.

By substituting Eqs. (29) and (30) into Eq. (28) and recognizing that the solid matrix modulus (K_s) is commonly several orders of magnitude larger than the pore volume modulus (K_P), we can obtain

$$\frac{d\varphi}{\varphi} = \left(\frac{1}{K} - \frac{1}{K_P}\right)(d\sigma^- - dp). \tag{31}$$

We assume that the volumetric variation of the porous medium satisfies the Betti–Maxwell reciprocal theorem $\partial V_b / \partial p \vdots_{\sigma^-} = \partial V_P / \partial \sigma^- \vdots_P$ [48], and we obtain Eq. (32).

$$K_P = \frac{\varphi}{\alpha} K. \tag{32}$$

The Biot's coefficient is considered one in this study, due to the soft coal seams; thus, we obtain $K_P = \varphi K$ [21]. By assuming $\varphi \ll 1\%$, Eq. (31) can be integrated as

$$\frac{d\varphi}{\varphi} = -\frac{1}{K_P}(d\sigma^- - dp), \tag{33}$$

and then $\int_{\varphi_0}^{\varphi}(d\varphi/\varphi) = -1/K_P(\int_{\sigma_0^-}^{\sigma^-} d\sigma^- - \int_{P_0}^{p} dp)$; thus, it can be expressed as

$$\frac{\varphi}{\varphi_0} = \exp\left\{-\frac{1}{K_P}[(\sigma^- - \sigma_0^-) - (p - p_0)]\right\}. \tag{34}$$

By substituting Eq. (34) into Eq. (25), the permeability of cleats is obtained as

$$\frac{k}{k_0} = \left(\frac{\varphi}{\varphi_0}\right)^3 = \exp\left\{-3C_f[(\sigma^- - \sigma_0^-) - (p - p_0)]\right\}. \tag{35}$$

where $C_f = 1/K_P$ is cleat volume compressibility.

For the conditions of uniaxial strain ($\varepsilon_{xx} = \varepsilon_{yy} = 0$ and $\sigma_{xx} = \sigma_{yy}$), the horizontal stress σ_{xx} or σ_{yy} is given from Eq. (15) and Eq. (20) as

$$\Delta\sigma_{xx} = \Delta\sigma_{yy} = \frac{\upsilon}{1-\upsilon}\Delta\sigma_{zz} + \frac{1-2\upsilon}{1-\upsilon}\Delta p + \frac{1-2\upsilon}{1-\upsilon}K(\varepsilon_s + \varepsilon_T). \tag{36}$$

We assumed that the reservoirs are under constant vertical stress ($\Delta\sigma_{zz} = 0$), and the changed mean stress becomes

$$\Delta\sigma^- = \frac{\Delta\sigma_{xx} + \Delta\sigma_{yy} + \Delta\sigma_{zz}}{3} = \frac{2(1-2\upsilon)}{3(1-\upsilon)}(\Delta p + \Delta K\varepsilon_s + \Delta K\varepsilon_T). \tag{37}$$

Substituting Eq. (37) into Eq. (35) and combining the relationship between C_f and φ_0 yield

$$\frac{k}{k_0} = \left(\frac{\varphi}{\varphi_0}\right)^3 = \exp\left\{\frac{3}{\varphi_0}\left[\frac{(1-2\upsilon)(1+\upsilon)}{E(1-\upsilon)}(p - p_0) - \frac{2}{3}\left(\frac{1-2\upsilon}{1-\upsilon}\right)((\varepsilon_s - \varepsilon_{s0}) + (\varepsilon_T - \varepsilon_{T0}))\right]\right\}. \tag{38}$$

Water and gas are coexisting in many CBM reservoirs. Therefore, the effective permeability, as a function of the relative permeability with the absolute permeability, represents the most significant parameter for the two-phase flow. The relative permeability models of Eqs. (39) and (40) at saturation S_w are widely used [52]. Gas slippage is not considered, and the gas/water endpoint relative permeability is calibrated in this study; a dynamic effective permeability model may be expressed as

$$k_{rg} = \left[1 - \left(\frac{S_w - S_{wr}}{1 - S_{wr} - S_{gr}}\right)\right]^2 \left[1 - \left(\frac{S_w - S_{wr}}{1 - S_{wr}}\right)^2\right], \tag{39}$$

$$k_{rw} = \left(\frac{S_w - S_{wr}}{1 - S_{wr}}\right)^4, \tag{40}$$

$$k_{eg} = kk_{rg}k_{rg0}, \tag{41}$$

$$k_{ew} = kk_{rg}k_{rw0}, \tag{42}$$

where k_{rg} represents the relative permeability of the gas and is dimensionless; k_{rw} is the relative permeability of water; k_{rg0} indicates the endpoint relative permeability of the gas; k_{rw0} denotes the endpoint relative permeability of water; S_{wr} represents the irreducible water saturation fraction; and S_{gr} is the residual gas saturation fraction.

2.2.5. Coupled Relationship. The hydraulic, mechanical, and thermal fields are defined by Eqs. (12), (13), (20), and (21), and the cross-coupling term of Eqs. (38), (39), and (40) complete the THM coupled model, as shown in Figure 2. These equations are implemented into the software of COMSOL *Multiphysics* to solve for reservoir evolution of CBM/ECBM recovery. Figure 3 shows the solution process for the model by COMSOL *Multiphysics*.

3. Model Validation and Simulation Schemes

3.1. Model Description. Four CO_2-ECBM field projects in China have been completed (three in the Qinshui Basin and one at the eastern margin of Ordos Basin), and the Qinshui Basin is one of the most representative commercial CBM basin [53]. In 2002, a pilot testing of CO_2-ECBM in deep unminable coalbed in Qinshui Basin was undertaken by Chinese Commerce Department and the Canadian International Development Agency [15]. The target formation is the Permian Shanxi formation #3 coal seam of uniform thickness (~6 m), high CBM content (28.9-30.5 m³/t), permeability (0.002-12.6 mD), burial depth (~472-972 m), and reservoir pressure (2.4-6.1 MPa) [54]. The main parameters for the basic geological model are shown in Table 1—mainly obtained from related literature. Vertical well spacing with *in situ* primary production is usually arranged on a rectangle pattern of 300×300 m as shown in Figure 4(a). Moreover, the multiwell pilot testing—an injection well—is located at the center of a near-square array of four production wells in a traditional five-spot pattern [55] (Figure 4(b)). Quarter of the near-regular five-spot pattern is represented
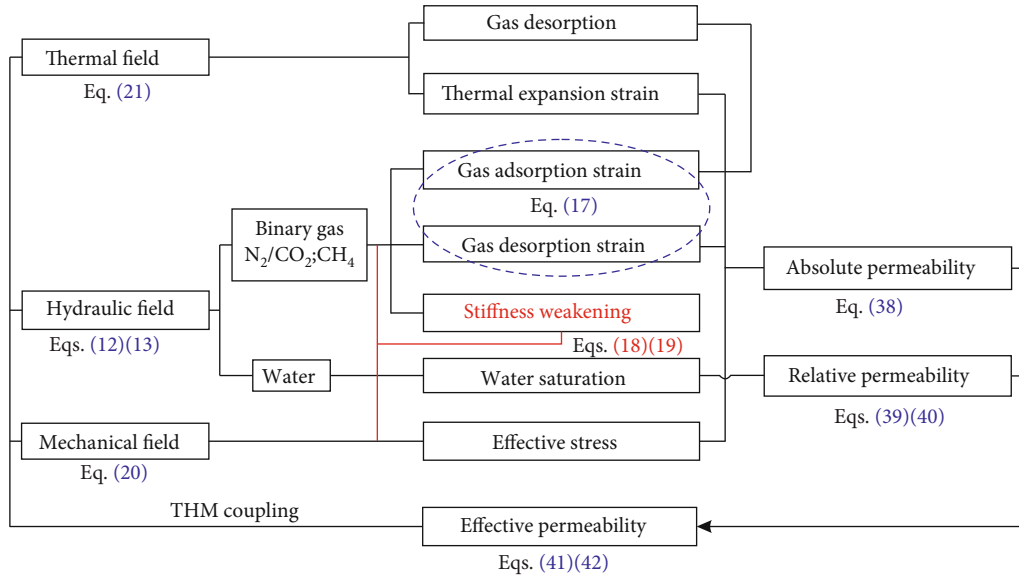
FIGURE 2: Interactions of multiple processes during ECBM recovery.

by a 150×150 m block to simulate the CO_2/N_2-ECBM pilot test (Figure 4(c)). The reference section (Line A-B) and three points (P1, P2, and P3) are used to investigate the reservoir parameters evolution. This study is performed in two parts by the proposed CBM simulation model. The established THM model is validated by using history matching of pressure depletion production of a typical production well and then implemented for the performance prediction of CO_2/N_2-ECBM production and CO_2 sequestration. Table 2 lists the parameters used in the study of model validation. Table 3 lists the related parameters for the simulation of CO_2/N_2-ECBM recovery.

3.2. Model Validation. History matching is used to conduct the model validation, and the field data is obtained from some scholars, who have reported the CBM production rate from an unstimulated production well subject to pressure deletion recovery *in situ* of Qinshui Basin. Unsurprisingly, the simulated gas production in Figure 5 is not perfectly consistent with the actual production shown, especially for the time of actual peak gas production (slightly lagging behind). This might be mainly attributed to permeability anisotropy, heterogeneity, and the single-phase flow of water during the dewatering stage (no gas production) in the field. Coincidentally, the average relative error of CH_4 production between this simulation and field data is ~16% (Figure 5), with the corresponding of values for the other study of 16.3% [43]. Note that, compared with the values of gas production rate, the shape of simulated gas production profile should be more concerned. Although the average relative error, both in this study and the literature, are consistent, the gas production profile of this research is more in agreement with the field profile. It indicates that the mathematical model of THM coupling can be used to simulate the primary CBM production, as well as extend the CO_2/N_2-ECBM production prediction.

4. Results and Analysis

4.1. Effect of Different Injection Gas on ECBM

4.1.1. CH_4 Recovery. During primary production and pure CO_2/N_2-ECBM recovery, CH_4 production rates all show a trend of rising first as the coalbed water continuously discharged, and then reduction (Figure 6(a)). The peak production rates for primary injection of CO_2 and N_2 are 304.6, 406.1, and 1615.1 m^3/day, with the corresponding time of 308, 906, and 423 days, respectively. Compared with primary production, injection of CO_2 and N_2 not only elevate CH_4 recovery rate (even up to 33.3% and 432%) separately but also delay the peak production rate. The cumulative CH_4 production for the projects of primary production and CO_2/N_2-ECBM recovery at 4000th day reach 0.68×10^6, 1.21×10^6, and 1.73×10^6 m^3, respectively (Figure 6(b)). Making the case of primary as a reference, the cumulative productions for CO_2/N_2-ECBM recovery are increased by 78.3% and 155.3%, separately. For primary production, the recovery ratio at 4000th day is 25.1%, with the corresponding values for CO_2/N_2-ECBM recovery of 44.8% and 62.7%, separately. Meanwhile, the enhancement factors, which are defined as the proportion of enhanced recovery ratio to that of primary production, are 1.78 and 2.5. All those state that the CH_4 recovery might be effectively enhanced by reactive gas (CO_2) or inert gas (N_2) injection, and the enhancement effect of N_2 injection is better than that of CO_2. However, an important issue cannot be ignored during enhanced recovery—CO_2/N_2 breakthrough, which may cause deterioration of produced gas purity and decrease the calorific value—thereby early well shutdown. Especially, N_2 breakthrough occurs shortly after the start of injection (~265 days), and it is attributed to lower dynamic viscosity and weak adsorption capacity of N_2 (Figure 7(b)). In contrast, the time of CO_2 breakthrough will be dramatically delayed (~1500 days) due to the larger
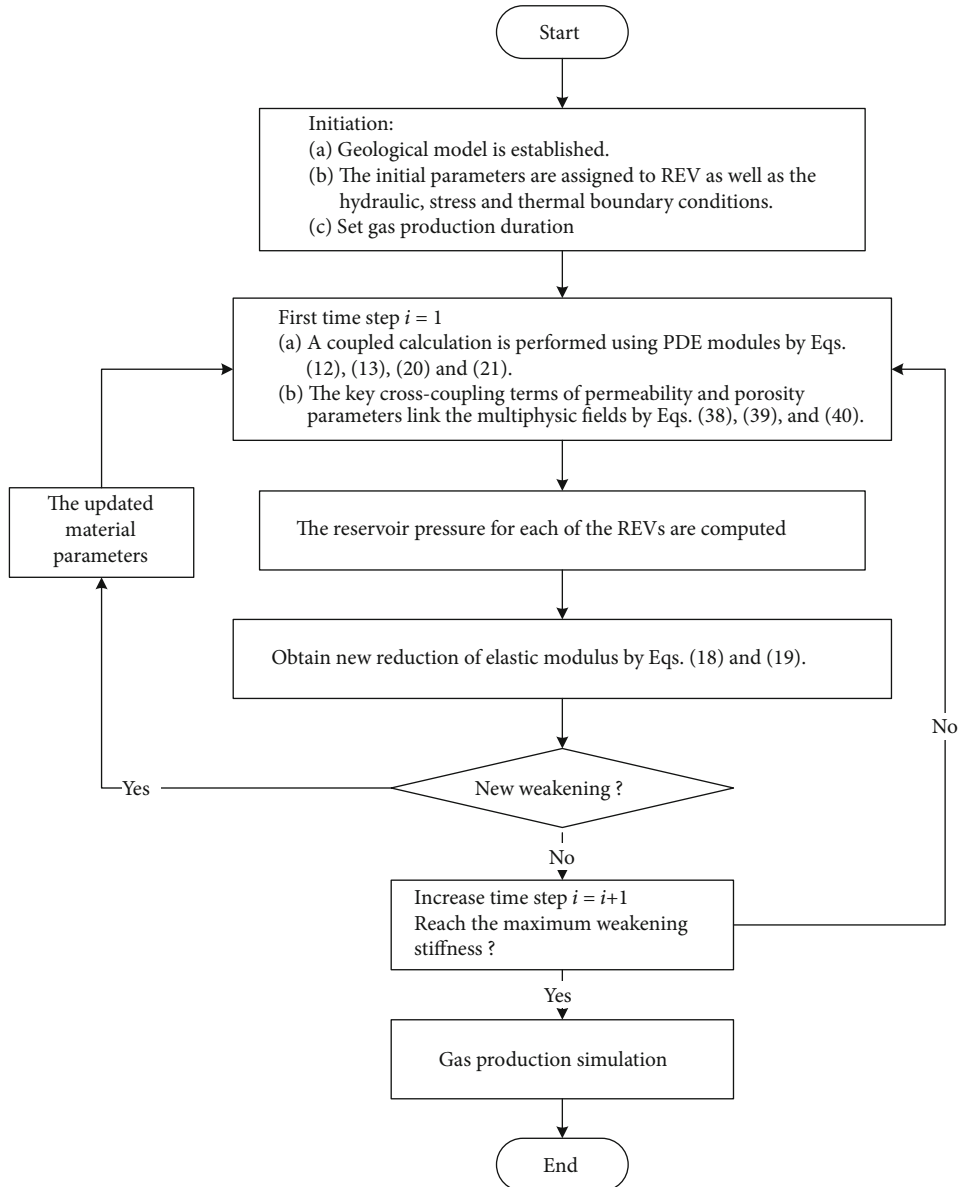
Figure 3: Solving process of THM coupled model for primary/ECBM production.

adsorption capacity decreasing the passing ability (Figure 7(a)). Therefore, there is a tradeoff between incremental CBM production and the earlier N_2 breakthrough. For instance, N_2 and CO_2 mixture injection could be applied to balance early N_2 breakthrough and pronounced matrix swelling induced by CO_2 adsorption and prolong the process of effective CH_4 recovery.

4.1.2. Permeability Ratio. Similar to the findings of previous studies [42–44], with the primary production continued, reservoir permeability at different reference points first decreases due to the increase of effective stress and then rebounds due to CH_4 desorption-induced matrix shrinkage (Figure 8(a)). With the approaching to the production well, permeability rebound appears earlier, and the ultimate permeability recovery is also the largest. The minimum permeability ratios at points P1, P2, and P3 are ~0.947 (672 days),

~0.949 (1117 days), and ~0.949 (1253 days), and these points reach the maximum values of ~1.045, ~1.012, and 1.001 at 4000 days.

However, the permeability evolution during CO_2/N_2-ECBM becomes more complex, compared to primary production. In the case of CO_2-ECBM, near the production well (P1), the permeability ratio evolution is similar to primary production in early time, while decreases dramatically with the arrival of CO_2 due to continued injection (Figure 8(b)). The minimum permeability ratio at point P1 is 0.54 at 4000 days. In the middle of the reservoir (P2), the permeability remains stable over the first 420 days due to the dual opposing effects—decreasing effective stress and matrix swelling—and then continuously decreases. Near the injection well, it is noted that the permeability first slightly increases due to the dominant factors of the reduction for effective stress and sharply declines due to CO_2

TABLE 1: Parameters for basic geological model.

| Parameter	Value	Remake	Parameter	Value	Remake
Dynamic viscosity of CH_4 (μ_{gi}, Pa s)	1.84×10^{-5}	[52]	Thermal conductivity of coal (λ_s, W/(m·K))	0.1913	[42]
Dynamic viscosity of water (μ_w, Pa s)	1.01×10^{-3}	[52]	Thermal conductivity of water (λ_w, W/(m K))	0.5985	[42]
Density of coal skeleton (ρ_s, kg/m^3)	1400	—	Thermal conductivity of CH_4 (λ_g, W/(m·K))	0.0301	[42]
Density of water at standard condition (ρ_w, kg/m^3)	1000	—	Isosteric heat of CH_4 adsorption (q_{st1}, kJ/Mol)	16.4	[42]
Thermal expansion coefficient of coal (α_T, 1/K)	2.4×10^{-5}	[52]	Thermal coefficients of gas adsorption (c_1, 1/T)	0.021	[52]
Langmuir-type strain coefficient of CH_4 (ε_{Li})	0.0128	[43]	Thermal coefficients of gas adsorption (c_2, 1/MPa)	0.071	[52]
Specific heat capacity of coal (C_S, J/(kg·K)	1350	[43]	Reference temperature for adsorption test (T_{ref}, K)	300	[42]
Specific heat capacity of water (C_W, J/(kg K)	4187	[42]	Adsorption time of CH_4 (τ_1, d)	0.2	[42]
Specific heat capacity of CH_4 (C_g, J/(kg·K)	2220	[42]	Initial water saturation (s_w)	0.85	—
Residual gas saturation (s_g)	0.05	[42]	Irreducible water saturation (s_{wr})	0.4	[42]
Capillary pressure (p_{cgw}, MPa)	0.035	[42]	Initial reservoir temperature (T_0, K)	303.5	—
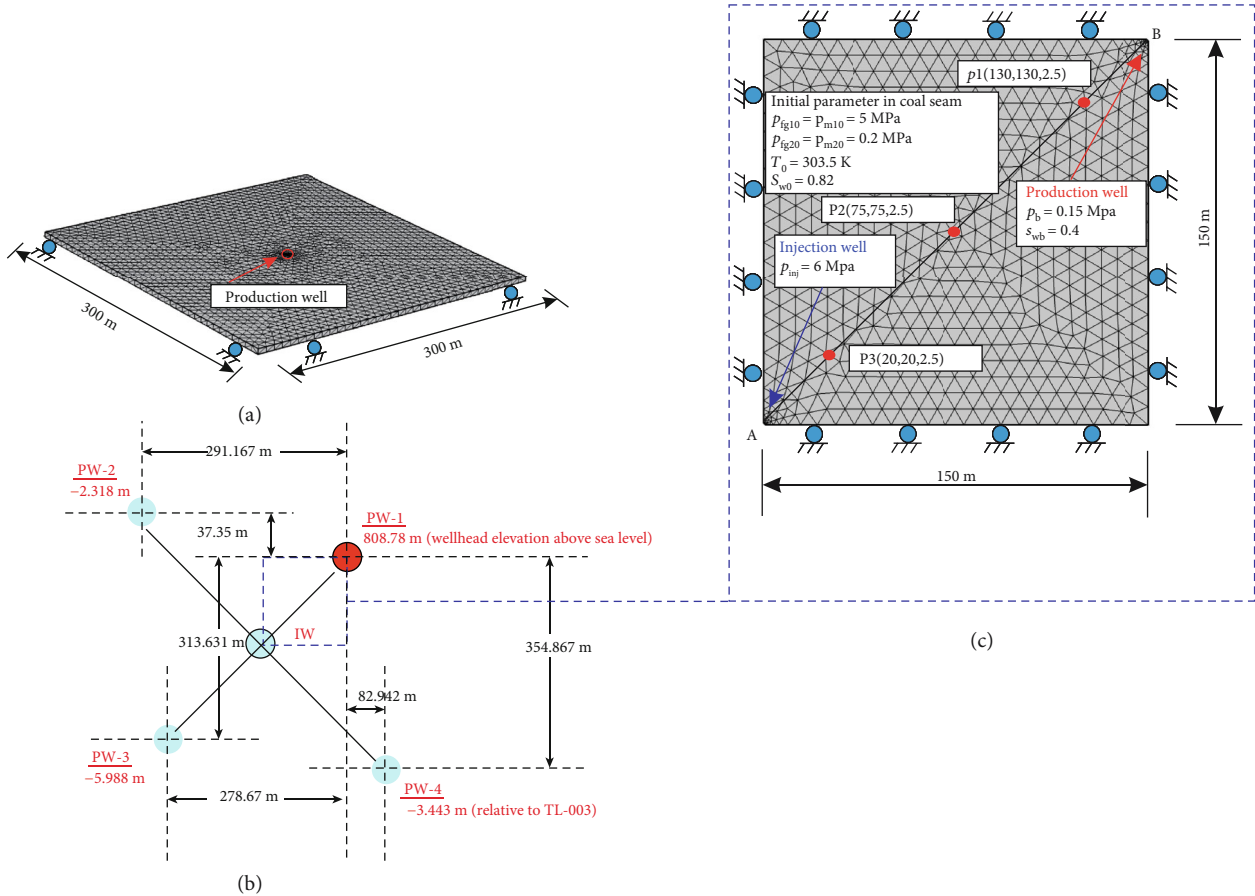
FIGURE 4: Geological model for numerical simulation. (a) Model validation. (b) Five-spot pattern [55]. (c) Model for ECBM production.

adsorption induced by matrix swelling soon afterwards. In the case of N_2-ECBM, permeability ratios at different points all show a trend of rising to a peak first due to the net matrix shrinkage and higher total pressure remaining, and then reduction to a stable value due to total reservoir pressure depletion (Figure 8(c)). The maximum permeability ratios for points P1, P2, and P3 are 2.3, 2.7, and 3.1, and these points reach a stable value of 2, 2.2, and 2.4,

TABLE 2: Key parameters for model validation.

Parameter	Value	Remake	Parameter	Value	Remake
Initial permeability (k_0, mD)	3.8	[54]	Elastic modulus of coal seam (E, GPa)	2.7	[42]
Porosity of fracture (φ_f, %)	0.6	[54]	Poisson's ratio of coal (v)	0.35	[42]
Langmuir pressure constant of CH_4 (P_{L1}, MPa)	1.99	[54]	Langmuir volume constant of CH_4 (V_{L1}, m^3/kg)	0.030	[54]
Initial CH_4 pressure in fracture (P_{fg10}, MPa)	5	[54]	Initial CH_4 pressure in matrix (P_{mg10}, MPa)	5	[54]

TABLE 3: Key parameters for ECBM recovery.

| Parameter	Value	Remake	Parameter	Value	Remake
Initial permeability (k_0, mD)	0.5	—	Elastic modulus of coal seam (E, GPa)	2.7	[42]
Porosity of fracture (φ_f, %)	0.4	—	Poisson's ratio of coal (v)	0.35	[42]
Dynamic viscosity of CO_2 (μ_{g1}, Pa s)	2.22×10^{-5}	[52]	Langmuir pressure constant of CO_2 (P_{L2}, MPa)	1.38	[42]
Dynamic viscosity of N_2 (μ_{g2}, Pa s)	1.78×10^{-5}	[52]	Langmuir volume constant of CO_2 (V_{L2}, m^3/kg)	0.0447	[42]
Langmuir-type strain coefficient of CO_2 (ε_{L2})	0.0237	[42]	Langmuir pressure constant of N_2 (P_{L2}, MPa)	2.61	[43]
Langmuir-type strain coefficient of N_2 (ε_{L2})	0.0058	[43]	Langmuir volume constant of N_2 (V_{L2}, m^3/kg)	0.0146	[43]
Adsorption time of CO_2 (τ_2, d)	4.34	[43]	Langmuir pressure constant of CH_4 (P_{L1}, MPa)	2.07	[42]
Adsorption time of N_2 (τ_2, d)	4.34	[43]	Langmuir volume constant of CH_4 (V_{L1}, m^3/kg)	0.0256	[42]
Thermal conductivity of CO_2 (λ_{g1}, W/(m K))	0.0137	[42]	Isosteric heat of CO_2 adsorption (q_{st2}, kJ/Mol)	19.2	[42]
Thermal conductivity of N_2 (λ_{g2}, W/(m K))	0.0262	[43]	Isosteric heat of N_2 adsorption (q_{st2}, kJ/Mol)	12.8	[43]
Specific heat capacity of CO_2 (C_{g1}, J/(kg K))	844	[42]	Specific heat capacity of N_2 (C_{g2}, J/(kg K))	1040	[43]
Initial CH_4 pressure in fracture (P_{fg10}, MPa)	5	[54]	Initial CH_4 pressure in matrix (P_{mg10}, MPa)	5	[54]
Initial CO_2 pressure in fracture (P_{fg20}, MPa)	6	—	Initial CO_2 pressure in matrix (P_{mg20}, MPa)	6	—
Initial N_2 pressure in fracture (P_{fg20}, MPa)	6	—	Initial N_2 pressure in matrix (P_{mg20}, MPa)	6	—
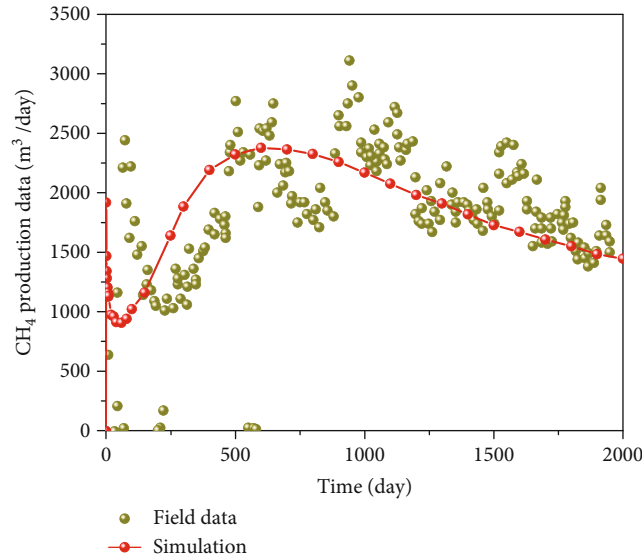
FIGURE 5: History matching for pressure deletion production in Qinshui Basin (field data from [56]).

respectively—illustrating that injection N_2 results in a greater increase of reservoir absolute permeability, compare with the case of CO_2 injection.

Near the production well, the increase of effective stress, matrix shrinkage, and swelling are the main controlling factors of permeability evolution, successively. Near the injection well, the decrease of effective stress and matrix swelling are the dominant factors, and then the final reservoir permeability will decrease to less than 60% of the initial value, which will further reduce the CO_2 injection rate. The net matrix shrinkage caused by N_2 injection and sustaining the total cleats pressure as the double positive effect factors make
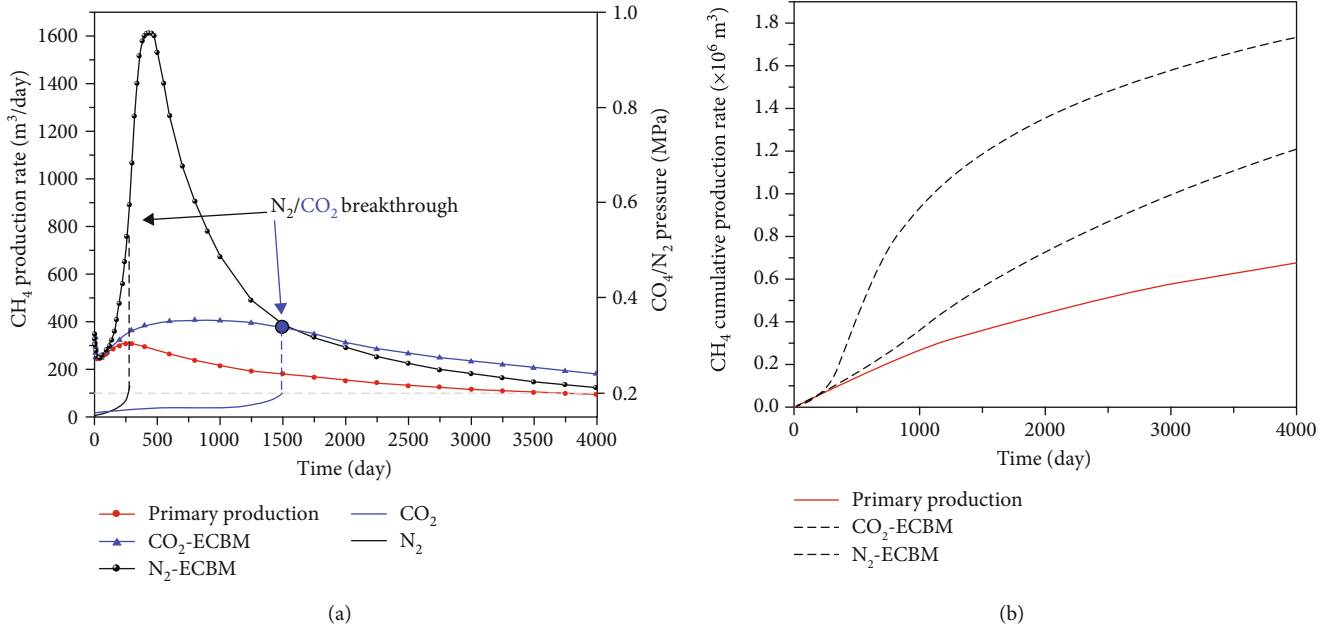
Figure 6: CH_4 production of primary CO_2 and N_2-ECBM recovery. (a) CH_4 production rate and CO_2/N_2 pressure distribution. (b) CH_4 cumulative production.
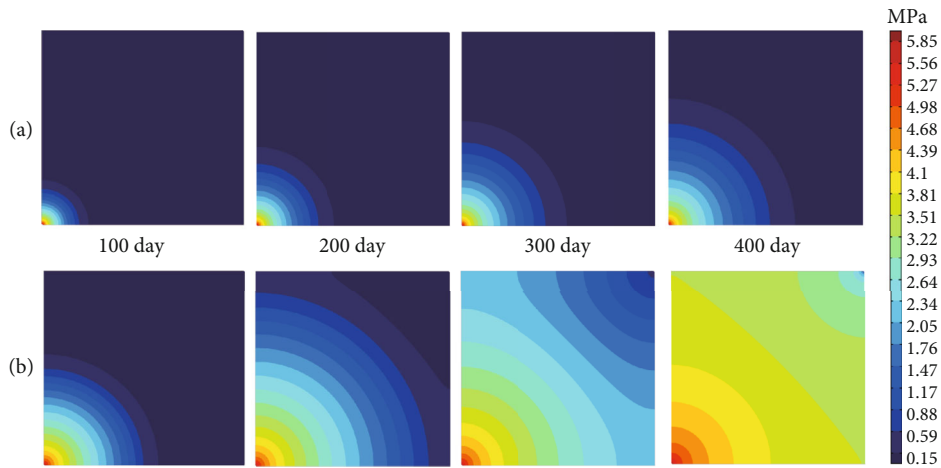

Figure 7: Distribution of injection pressure. (a) CO_2 partial pressure. (b) N_2 partial pressure.

the permeability increase rapidly. In the later stage, the permeability decreases slightly and tends to be stable due to the depletion of component CH_4. After 4000 days, the permeability of the reservoir will increase to more than 2 times of the initial value.

4.2. Effect of Coal Stiffness on ECBM. The simulation scheme for the effect of coal mechanical properties on ECBM is shown in Table 4.

4.2.1. CH_4 Production. During the primary CBM recovery under different mechanical properties of coal seam, CH_4 production rates all show a trend of sharply decreasing first due to the rapid release of free gas in the coal seam near the production well. Subsequently, CH_4 recovery rates first increase

in early time and then reduce at later time. The peak production rates for different scenarios of mechanical properties (from lower stiffness to higher stiffness) are 204, 226, and 250 m^3/day, respectively—illustrating that the higher stiffness of coal seams would result in a larger CH_4 production rate (Figure 9(a)). Making the case of lower stiffness of coal seam of CH_4 cumulative production at 4000 days ($0.57 \times 10^6 \, m^3$) as a reference, the corresponding CH_4 cumulative values under the medium and higher stiffness are increased by 14% ($0.65 \times 10^6 \, m^3$) and 22.8% ($0.7 \times 10^6 \, m^3$), separately (Figure 10(a)).

For CO_2-ECBM, the CH_4 recovery rate at early production is greater for the case of higher stiffness; however, the peak production rate for lower stiffness of coal seam would be elevated and delayed, subsequently (Figure 9(b)). The
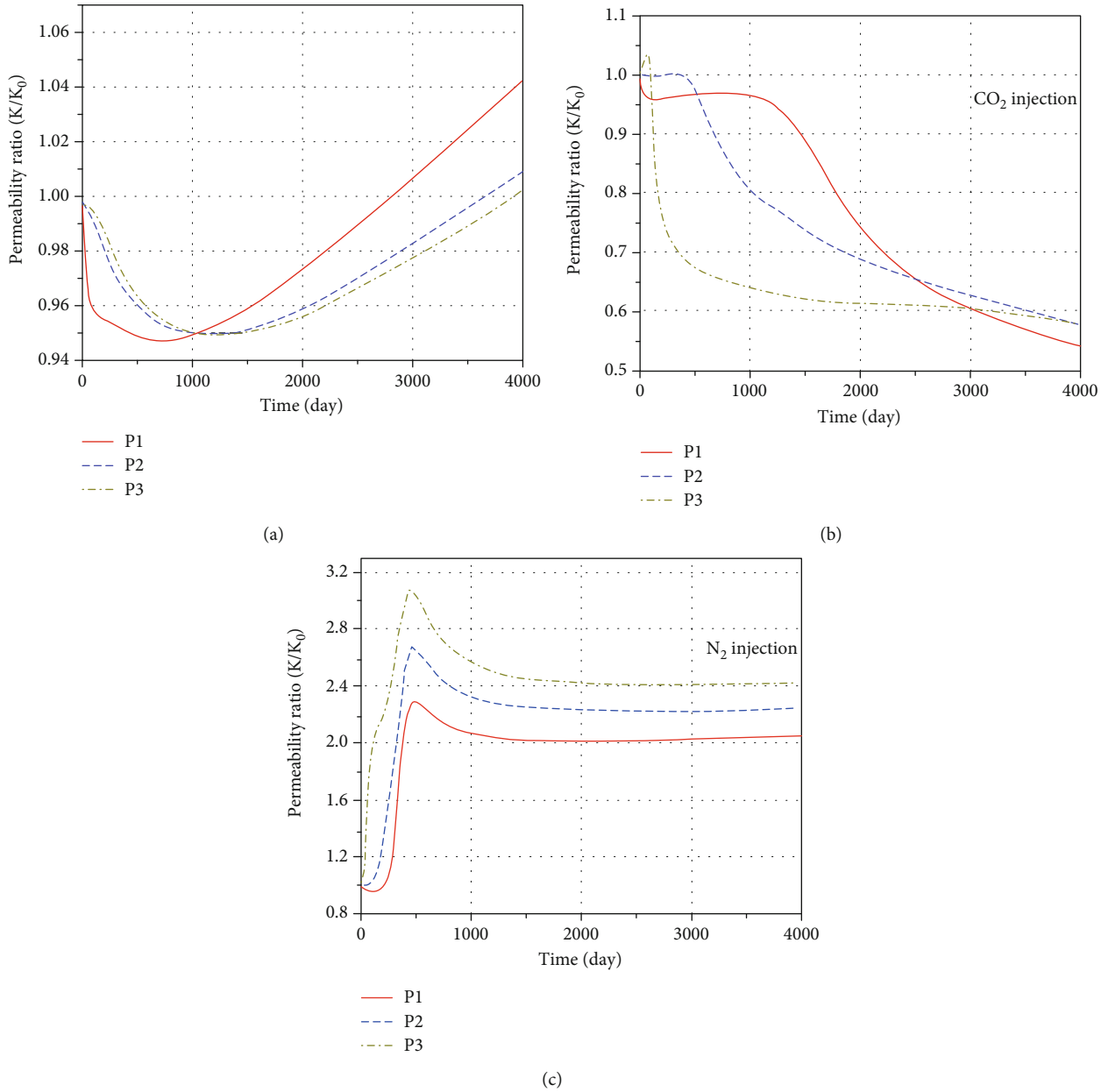
(a)

(b)

(c)

FIGURE 8: Permeability evolution of primary production and CO_2 and N_2 injection under different reference points (P1, P2, and P3).

TABLE 4: Numerical simulation schemes.

Scenario	Elastic modulus/GPa	Poisson's ratio
Lower stiffness	2.0	0.35
Medium stiffness	3.0	0.35
Higher stiffness	4.0	0.35

peak production rates for different scenarios of mechanical properties (from lower stiffness to higher stiffness) are 494.6 (1544 days), 348 (1580 days), and 325.1 m³/day (1150 days), respectively. The CH_4 cumulative production for soft (lower stiffness) coal seam within 1000 days is lower than that scenarios of medium and higher stiffness, while the value would rebound dramatically after 1000 days (Figure 9(b)). Making the case of harder coal seam CH_4 cumulative production as a reference (1.06×10^6 m³), by 4000th day, the corresponding CH_4 cumulative productions under the medium and lower stiffness are increased by 4.7% (1.11×10^6 m³) and 28% (1.36×10^6 m³), separately (Figure 10(b)).

As analyzed in "Effect of Different Injection Gas on ECBM," injection of N_2 can significantly enhance CBM production rate and cause early N_2 breakthrough; thus, we reduce the initial permeability to 0.1 mD. Different with CO_2-ECBM, with the decrease of coal seam stiffness, the peak production rate for N_2-ECBM would be elevated and advanced. The peak production rates for different scenarios
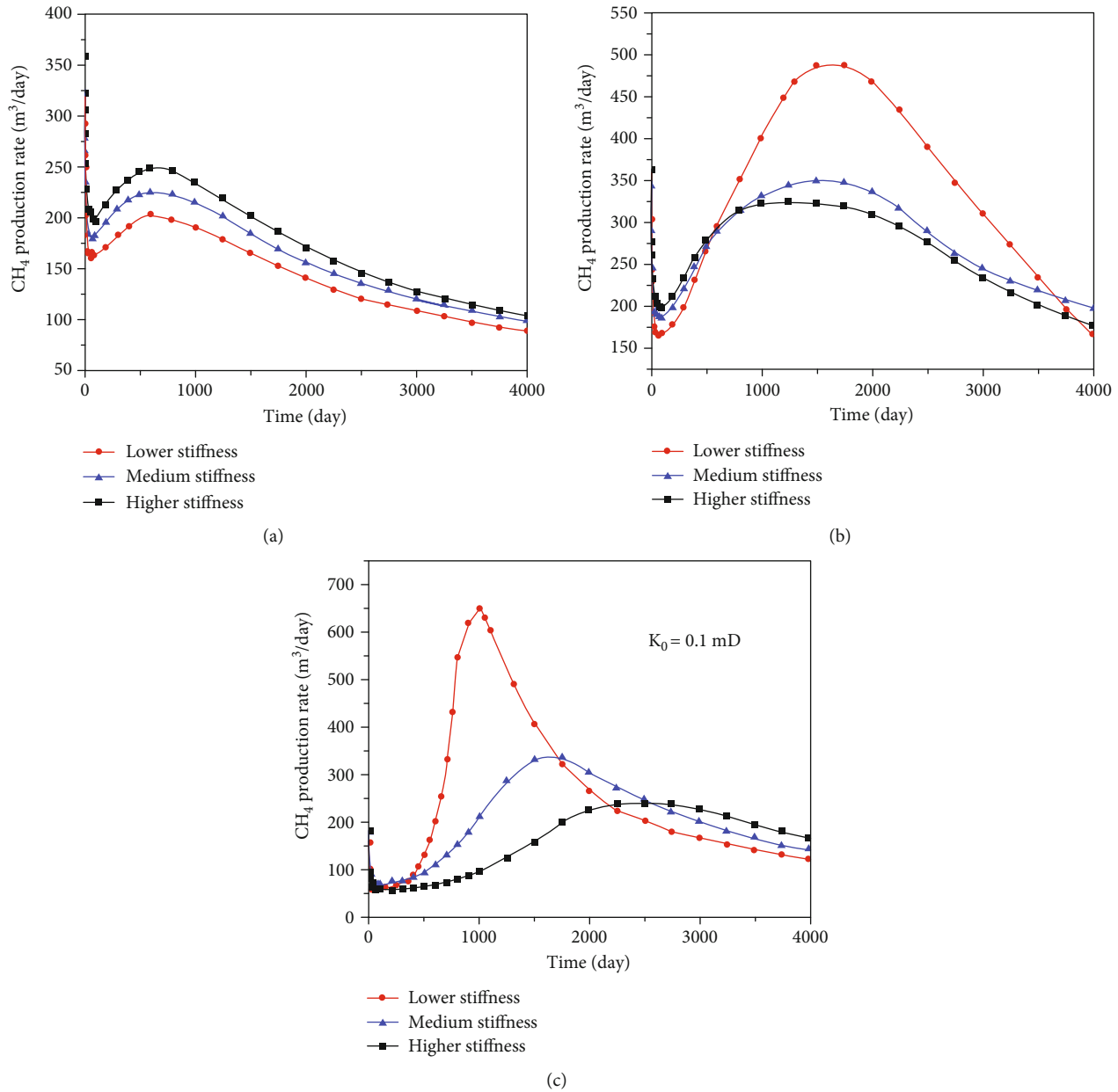
(a)

(b)

(c)

Figure 9: CH_4 production rate under different reservoir geomechanical properties. (a) Primary production. (b) CO_2-ECBM. (c) N_2-ECBM.

of mechanical properties (from lower stiffness to higher stiffness) are 494.6 (1544 days), 348 (1580 days), and 325.1 m³/day (1150 days), respectively (Figure 9(c)). However, it is noted that the production rate for harder coal seam is larger than those cases of medium and lower ones during the decline stage, and this phenomenon is similar to the primary CH_4 production. With the CBM recovery continued, CH_4 cumulative production for coal seams with different mechanical properties gradually increases. Making the case of harder coal seam CH_4 cumulative production at 4000th day as a reference (0.65×10^6 m³), the corresponding CH_4 cumulative productions under the medium and lower stiffness are increased by ~27.7% (0.83×10^6 m³) and ~55.4% (1.01×10^6 m³), separately (Figure 10(c))—illustrating that

N_2-ECBM in softer coal seam is more favorable. Compared with primary recovery and CO_2-ECBM, N_2-ECBM is more sensitive to the stiffness of coal seam.

4.2.2. CO_2 Storage. The CO_2-ECBM project not only recovers additional CBM in unminable coal seams—utilizing CO_2 displacement and sweeping—but also effectively sequesters greenhouse gas. The CO_2 storage rates first increase and then decline as the coalbed water continuously discharged. With the decrease of coal seam stiffness, the peak storage rates are elevated and delayed (Figure 11(a)). The peak CO_2 storage rates of lower, medium, and higher stiffness CBM reservoirs are ~1132, ~687, and~580.5 m³/day, respectively, appearing at ~1610, 1580, and 1397 days.
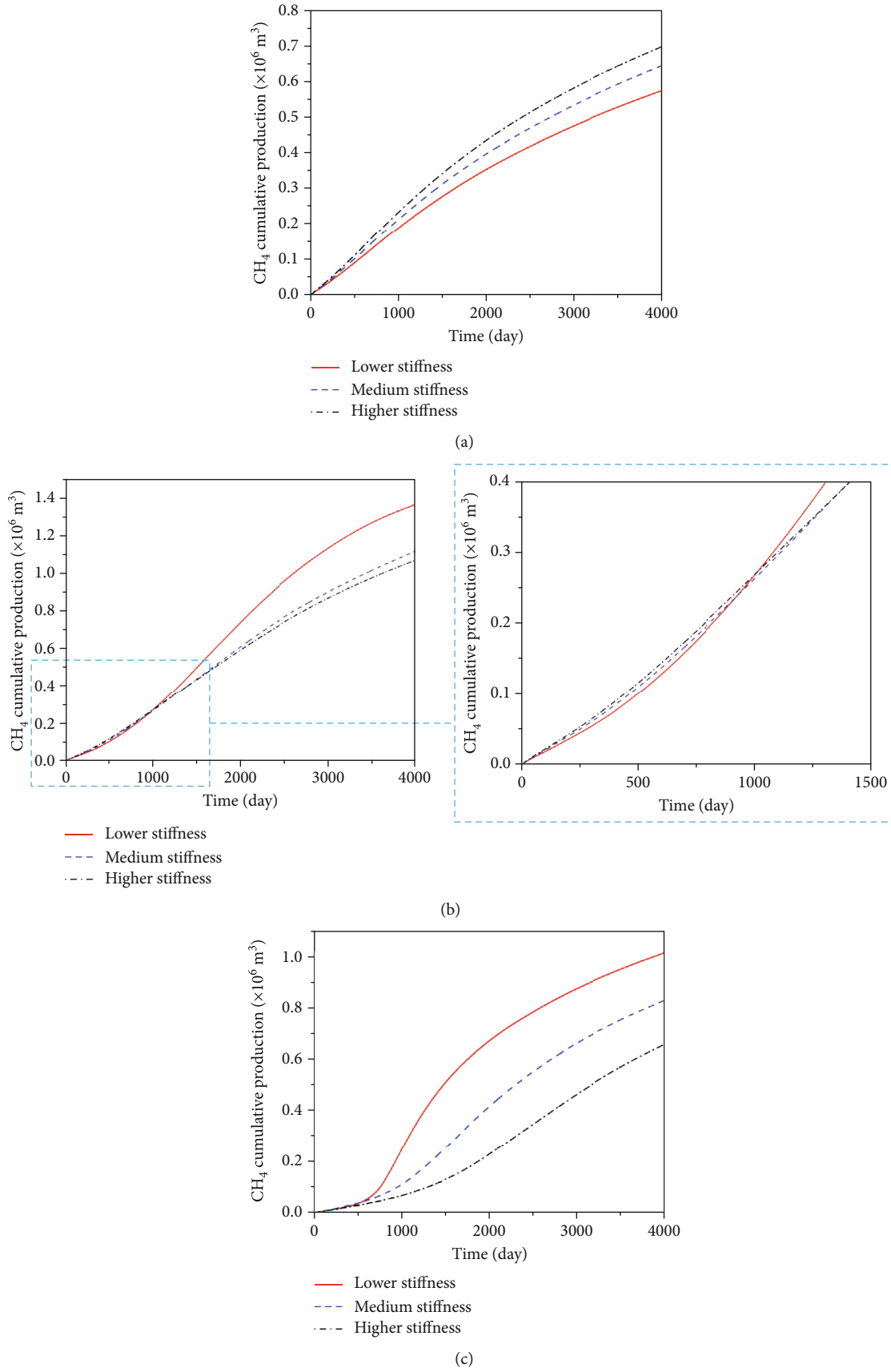
(a)

(b)

(c)

FIGURE 10: CH$_4$ cumulative production under different reservoir geomechanical properties. (a) Primary production. (b) CO$_2$-ECBM. (c) N$_2$-ECBM.
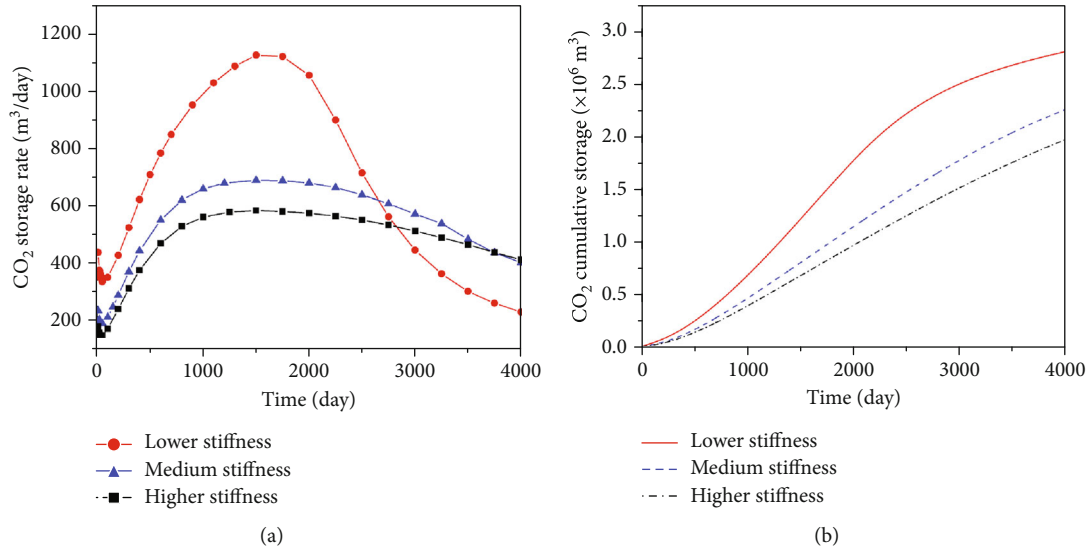
FIGURE 11: CO_2 storage of different stiffness of coal seams. (a) Storage rate. (b) Cumulative storage.
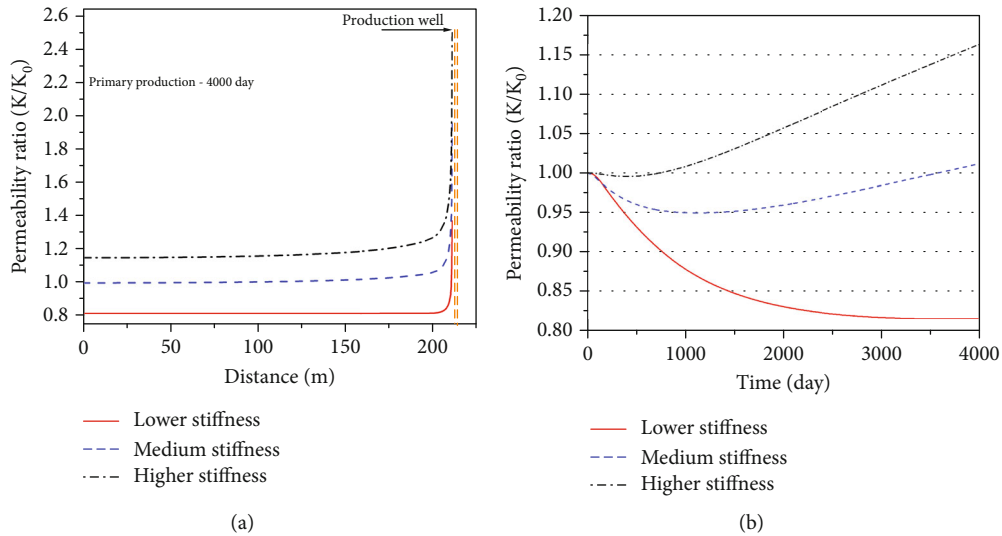

FIGURE 12: Permeability evolution within CBM reservoir during primary production. (a) Evolution of permeability ratio along reference section A-B. (b) Evolution of permeability ratio at reference point (P2).

Although, the CO_2 storage rate of lower stiffness CBM reservoirs is larger than the other scenarios during dewatering and stable production stage, it would decrease sharply at decline stage and even much lower than the other scenarios after 2750 days. The CO_2 cumulative storage decrease from the lower stiffness to the medium stiffness, and then higher stiffness, with a maximum cumulative storage of the three scenarios reaching approximately 2.8×10^6, 2.25×10^6, and $1.96 \times 10^6 \, \text{m}^3$ at the 4000th day (Figure 11(b)), respectively. Making the case of harder coal seam of CO_2 cumulative storage as a reference, the corresponding cumulative storage under the medium and lower stiffness is increased by ~14.8% and ~42.9%, separately, indicating a significant and practicability CO_2 storage capacity within the soft coal seam.

4.2.3. Permeability Evolution. For the project of primary production, due to the small decline in temperature and princi-

pal matrix shrinkage over the negative effect of increased effective stress, matrix shrinkage dominates the evolution of permeability near the production well, thus leading to an increase in permeability. On one hand, the dominant factor (matrix shrinkage) is gradually weakened as it is far away from the production well. On the other hand, with the decrease of coal seam stiffness, the enhanced stress sensibility of coal permeability results in lower permeability ratio distribution within CBM reservoir (Figure 12(a)). For instance, the permeability ratio of the entire soft coal seam is almost below the initial permeability during the whole production process and even decreases by 20%. In contrast, the reservoir permeability for medium and higher stiffness coal seams would exceed their corresponding initial values at 4000th day. Making the point P2 as a reference, the higher stiffness of coal seam and the earlier permeability rebound and recovery appear (Figure 12(b)). The minimum permeability ratios
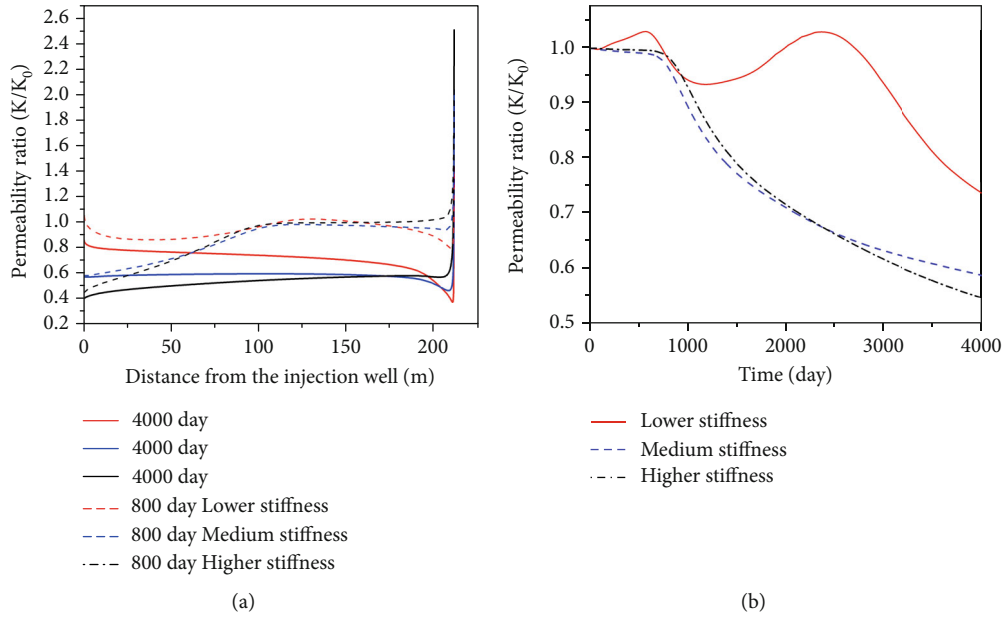
(a)

(b)

FIGURE 13: Permeability evolution within CBM reservoir during CO2-ECBM production project. (a) Evolution of permeability ratio along reference section A-B. (b) Evolution of permeability ratio at reference point (P2).
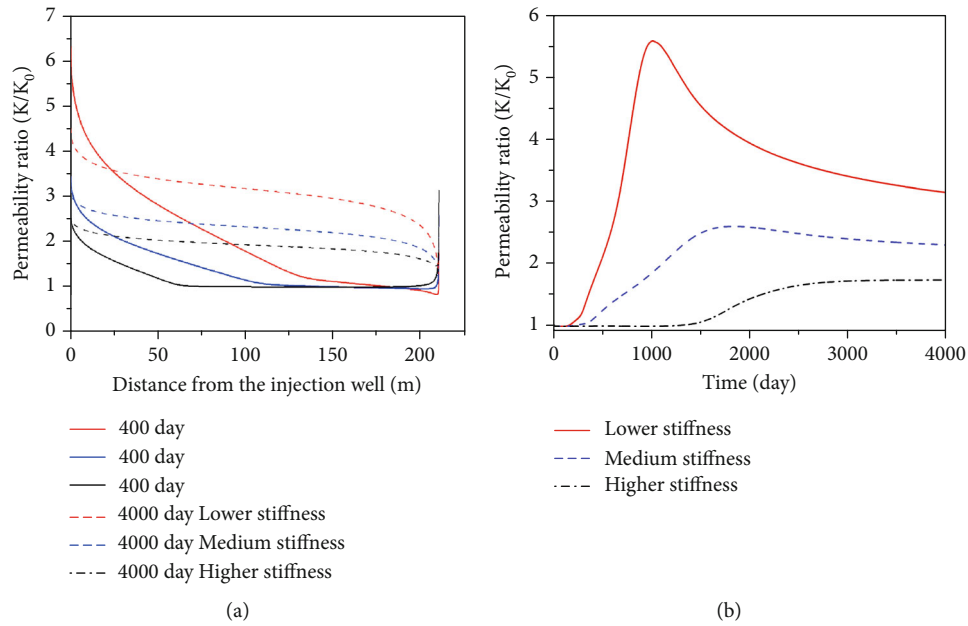

(a)

(b)

FIGURE 14: Permeability evolution within CBM reservoir during N_2-ECBM. (a) Evolution of permeability ratio along reference section A-B. (b) Evolution of permeability ratio at reference point (P2).

(permeability rebound) of higher and medium stiffness CBM reservoirs are ~0.99 (at 370 days) and ~0.95 (at 1100 days), and these reach a maximum ratio of 1.16 and 1.01, separately, at 4000 days. However, the permeability ratio of soft coal seam decreases dramatically over time, from 1 to 0.81 (at 4000 days), and there is no rebound or recovery of permeability due to the dramatically negative effect of increased effective stress.

For the project of CO_2-ECBM recovery, permeability evolution around the production well is similar to primary CH_4 recovery. Conversely, near the injection well, CO_2 injections cause the increase of reservoir pressure, reduce the effective stress, and then weaken the significant matrix swelling induced by CO_2 adsorption. Therefore, the softer the coal seam is, the higher permeability ratio would reach (Figure 13(a)). In addition, matrix swelling still dominates the evolution of permeability, especially for medium and higher stiffness coal seams; thus, reservoir permeability drops sharply during the whole CO_2-ECBM production project. Making the point P2 as a reference, the permeability ratio of medium and higher stiffness of coal seam first decreases slightly due to the increase of effective stress and
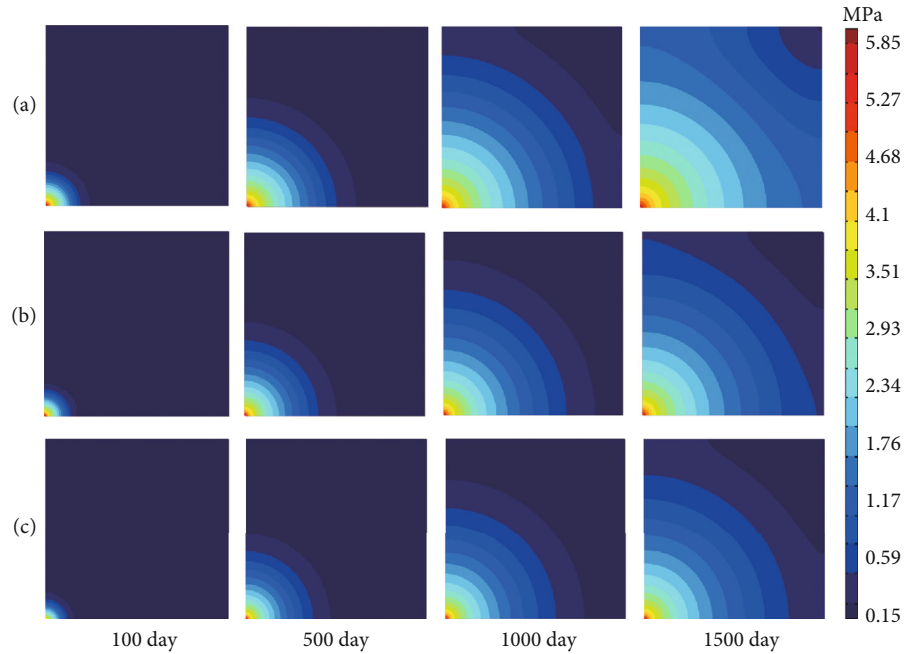
FIGURE 15: CO_2 migration within different stiffness of coal reservoir. (a) Lower stiffness. (b) Medium stiffness. (c) Higher stiffness.
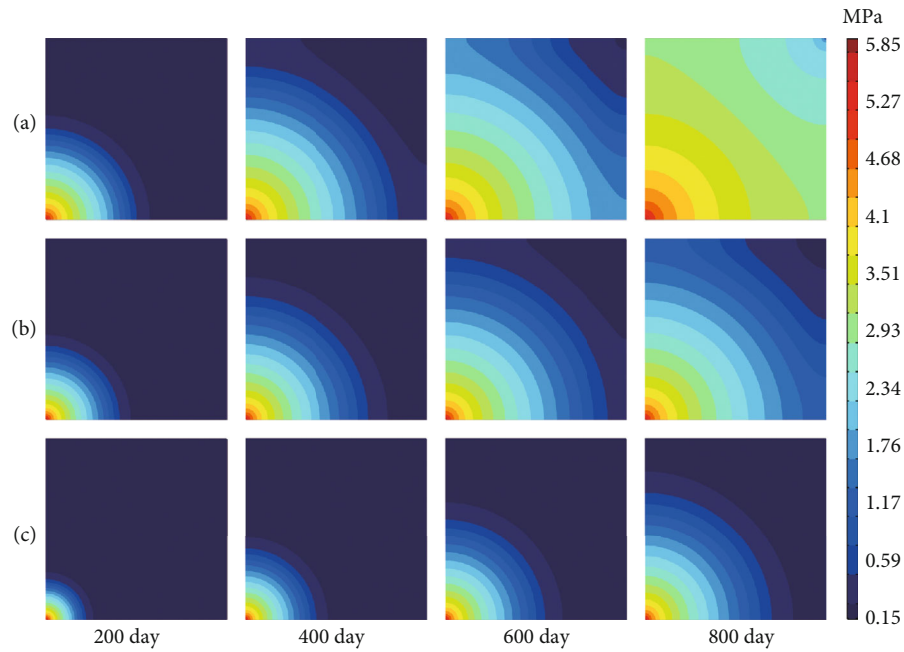

FIGURE 16: N_2 migration within different stiffness of coal reservoir. (a) Lower stiffness. (b) Medium stiffness. (c) Higher stiffness.

then reduces sharply due to CO_2 arrival (Figure 13(b)). However, the permeability ratio curves of soft coal seam exhibit undulated shape due to the more sensitive effect of effective stress (Figure 13(b)). Compared to hard coal seams, the permeability of soft one is increased by ~35.1% at 4000th day.

For the project of N_2-ECBM recovery, the permeability evolution is simple due to net matrix shrinkage. Near the production well, the permeability distributions under differ-ent scenarios are also similar to CO_2-ECBM and primary

production, before N_2 breakthrough. With approaching the injection well and N_2 injection continued, double positive effects—net matrix shrinkage and reduction of effective stress—dominate the permeability evolution; thus, reservoir permeability would increase dramatically, exhibiting the softer the coal seam, the higher the permeability (Figure 14(a)). Compared with hard coal seams, the permeability of soft one is increased by ~63.1% at 4000th day (Figure 14(b)).

Congruent with those previous studies [57, 58], the elas-tic modulus of the coal seam has a significant effect on the
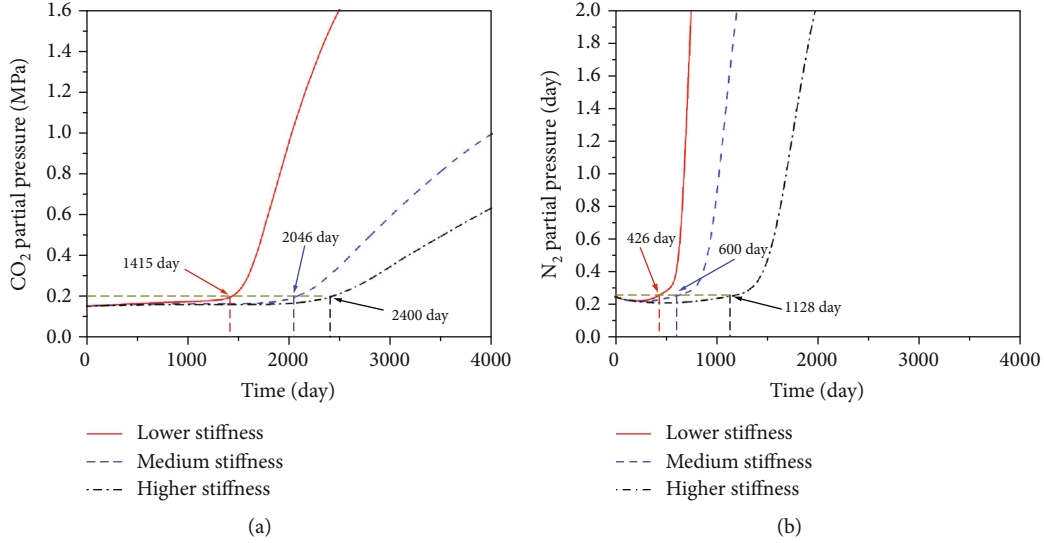
FIGURE 17: CO_2/N_2 partial pressure evolution. (a) CO_2-ECBM. (b) N_2-ECBM.
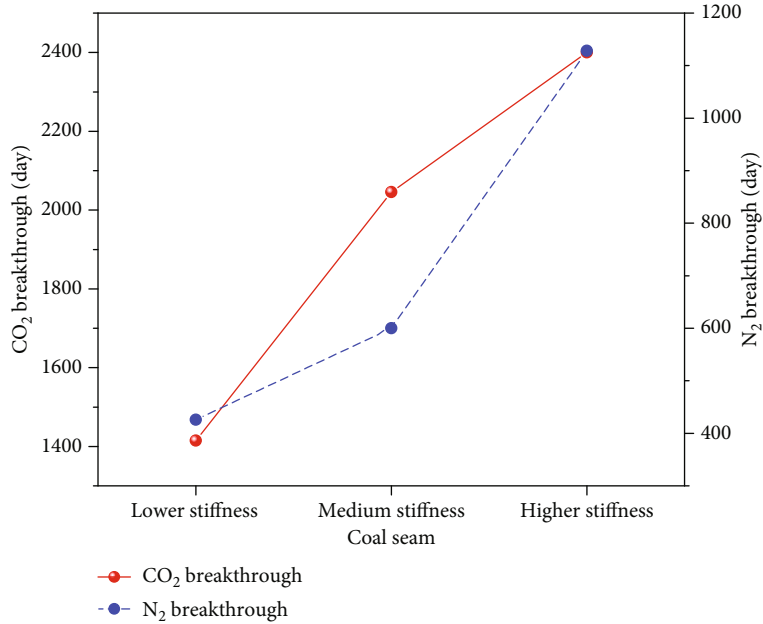

FIGURE 18: CO_2 and N_2 breakthrough of different stiffness of coal seams.

permeability within the reservoir. It can be illustrated that fluid injection into a more deformable reservoir (lower elastic modulus) opens up the fractures more easily and then results in a higher value of permeability, compared to a hard reservoir (with larger modulus).

4.2.4. CO_2/N_2 Breakthrough. With the rising stiffness of coal seam, the migration rates of CO_2 and N_2 gradually decrease in CBM reservoirs (Figures 15 and 16). CO_2 breakthrough for lower, medium, and higher stiffness coal seams appears at 1415, 2046 and 2400 days, respectively, when the CO_2 partial pressure begins to increase (Figure 17(a)). The corresponding values for N_2 breakthrough are 426, 600, and 1126 days, respectively (Figure 17(b)). It is noted that CO_2 breakthrough is delayed slightly from the condition of

TABLE 5: Numerical simulation schemes.

The maximum weakening degree	E_{int} (GPa)	ΔE_{max} (GPa)	P_E (MPa)
10%		0.3	
20%	3.0	0.6	1.5
30%		0.9	

medium stiffness to higher stiffness for CO_2-ECBM. In contrast, N_2 breakthrough is delayed sharply under the same condition (Figure 18). The major reason for this phenomenon could be attributed to the double positive effects of permeability evolution on N_2 injection and the single positive effect on CO_2 injection caused by permeability change. The
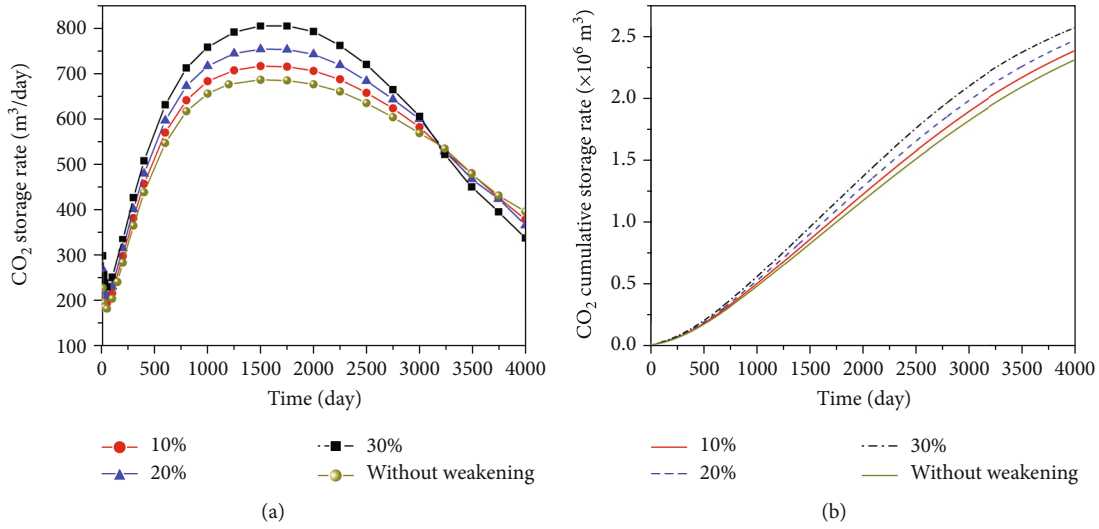
FIGURE 19: CO_2 storage rate and cumulative storage under different weakening degrees. (a) CO_2 storage rate. (b) CO_2 cumulative storage.
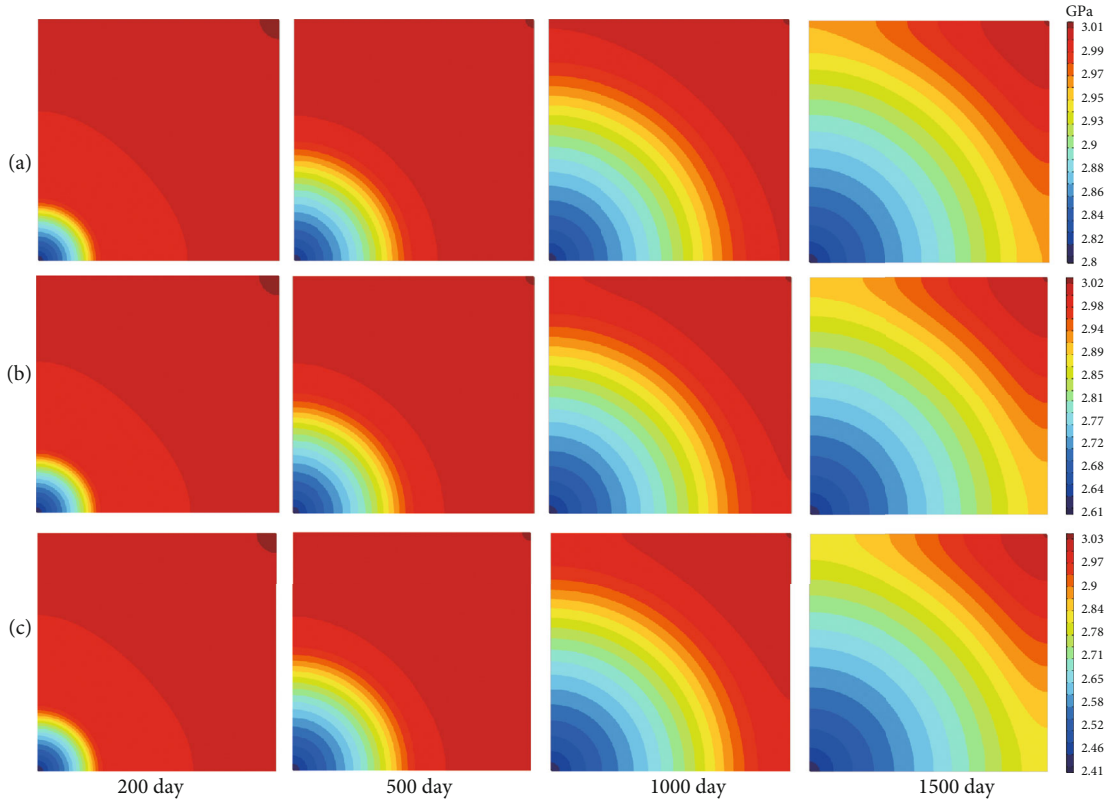

FIGURE 20: The distribution of elastic modulus in CBM reservoirs during CO2 injection. (a) 10%; (b) 20%; (c) 30%.

increase of stiffness restrains the double or single positive effect on permeability evolution during N_2 or CO_2 injection. Note that the restraint for CO_2 injection are weakened due to the dominant factor of matrix swelling induced by CO_2 adsorption. However, the restraints for N_2 injection are significant due to the potential for transforming from double positive effect to singe positive effect—the net matrix shrinkage.

4.3. Effect of CO_2 Interaction Induced Mechanical Property Alteration on CO_2-ECBM. Compared with N_2/CH_4 adsorption, CO_2 adsorption not only induces matrix swelling but also accompanies the reductions in stiffness and strength and then shows a significant effect on permeability changes and CO_2 storage. CO_2 storage and reservoir permeability evolution are investigated due to the reduction in stiffness in this paper. The simulation scheme is shown in Table 5.
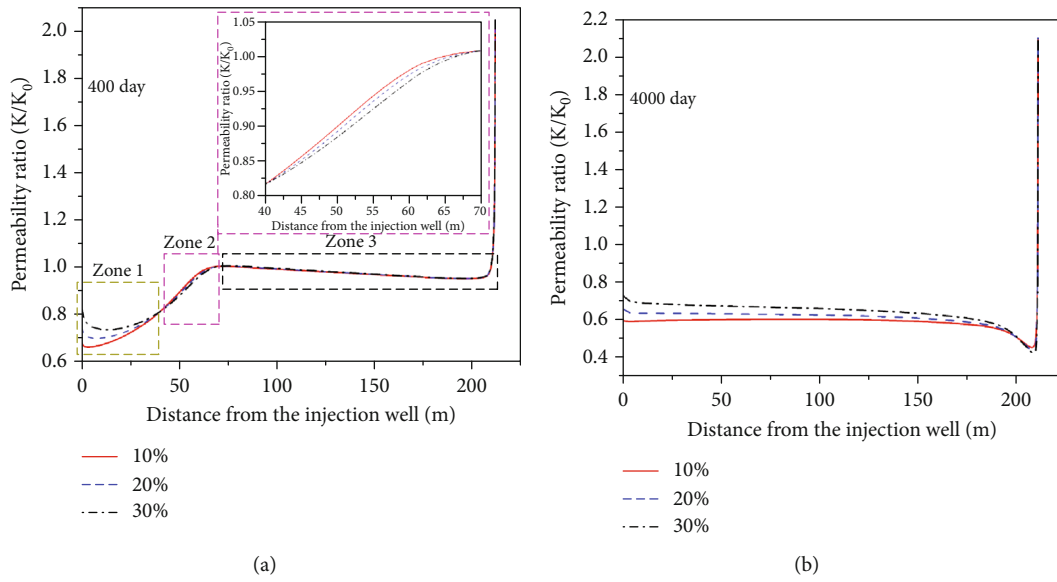
FIGURE 21: Evolution of permeability ratio along reference section A-B. (a) Permeability ratio at 400 days. (b) Permeability ratio at 4000 days.
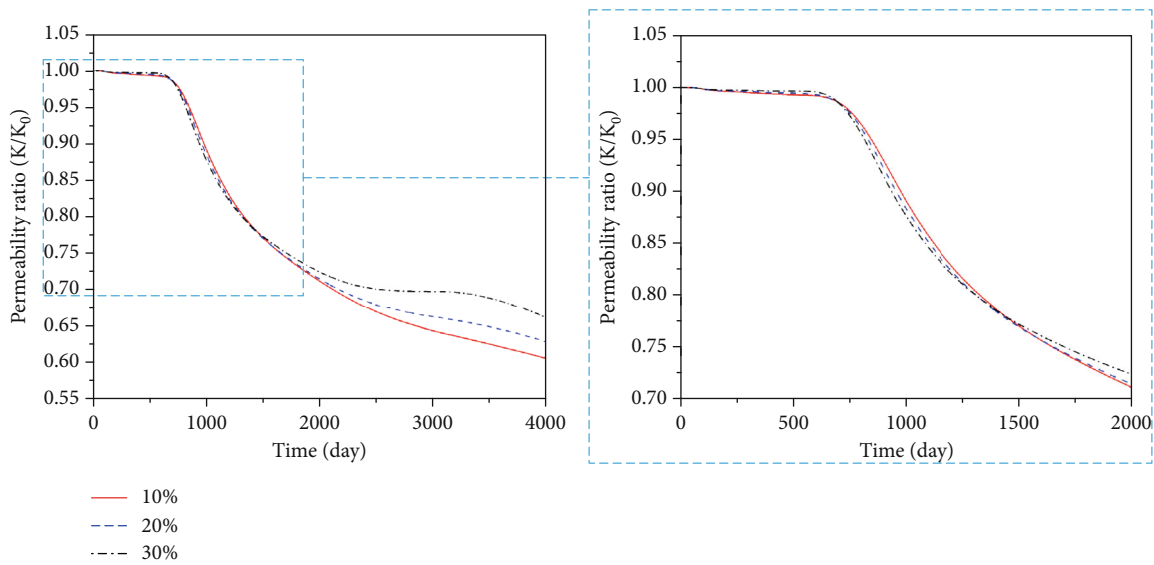

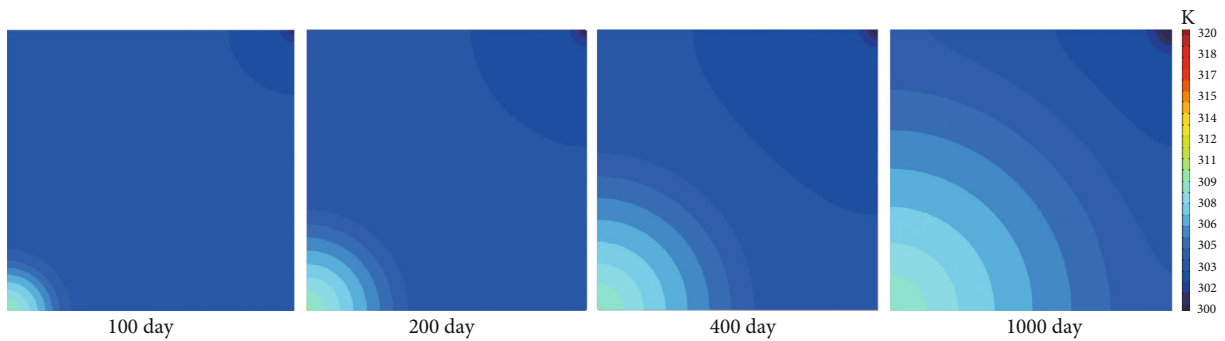FIGURE 22: Evolution of permeability ratio at the reference point (P2).

FIGURE 23: Distribution of temperature during hot CO_2 injection (320 K).
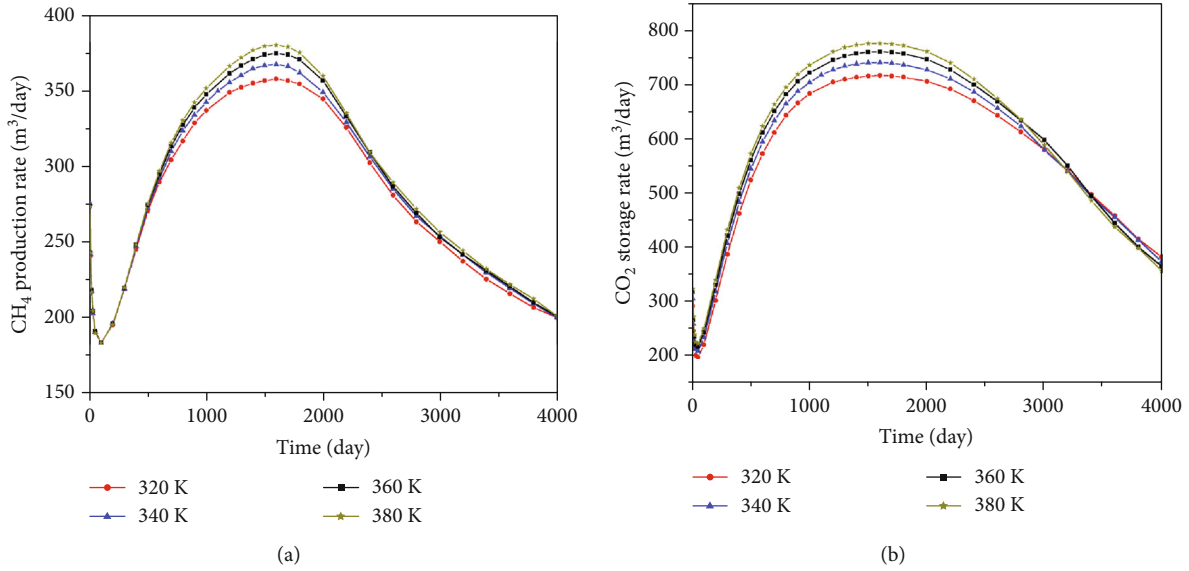
Figure 24: Evolution of CH_4 production and CO_2 storage. (a) CH_4 production rate. (b) CO_2 storage rate.
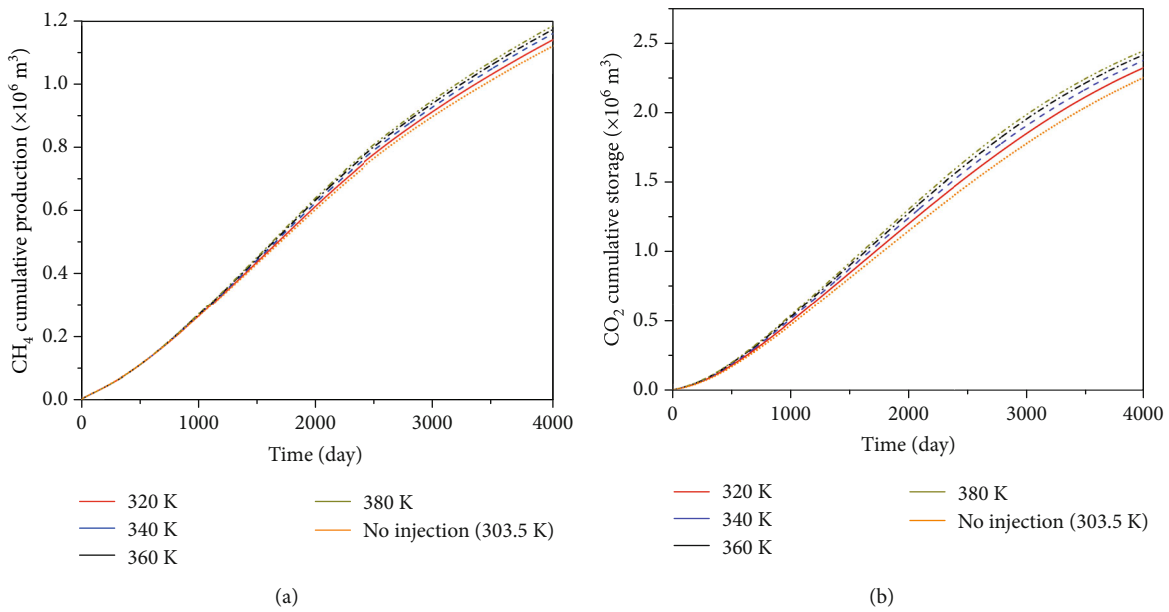

Figure 25: CH_4 cumulative production and CO_2 cumulative storage under different injection temperatures. (a) CH_4 cumulative production. (b) CO_2 cumulative storage.

4.3.1. CO_2 Storage. With the increase of the weakening degree of coal seam stiffness, both CO_2 storage rate and CO_2 cumulative storage all show a trend of increase. The peak CO_2 storage rates of no stiffness weakening and weakening degree from 10% to 30% are ~684.8, ~714.9, ~753.5, and 804.2 m³/day, respectively (Figure 19(a)). The CO_2 cumulative storage of the conditions gradually increases, with a maximum cumulative storage reaching approximately 2.25×10^6, 2.32×10^6, 2.40×10^6, and 2.50×10^6 m³ at the 4000th day, respectively (Figure 19(b)). Making the case of no weakening as a reference, the corresponding cumulative storage under the weakening degree from 10% to 30% is increased by

~3.1%, ~6.5%, and 11.1% separately, indicating the higher the weakening degree, the better the CO_2 storage.

4.3.2. Permeability Ratio. CO_2 interaction with coal seam would induce mechanical characteristics alterations, such as elastic modulus—which controls the stiffness of the coal cleat systems. Reduction in elastic modulus can alleviate the sharp decline of permeability caused by CO_2 adsorption due to the elevated positive effect of effective stress decrease. The process is positive feedback—CO_2 injection decreases the elastic modulus and then causes a large injection volume, and a large injection volume would also cause a large scale and
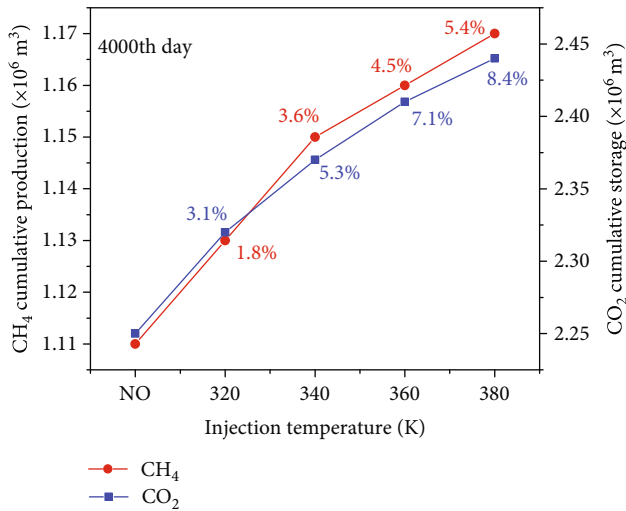
FIGURE 26: The cumulative CH_4 production and CO_2 injection.

degree of weakening on coal seam stiffness. The lower elastic modulus is firstly distributed near the injection well and then propagates to the production well subsequently. With the increase of the maximum weakening degree of coal seam stiffness, sharper reduction of coal seam stiffness appeared (Figure 20). Variation of stiffness will affect the dynamic permeability. The evolution of permeability ratio along the reference section A-B is divided into three zones before CO_2 breakthrough (Figure 21(a)). Making the case of 400th day of production, Zone 1 represents the dominant factor caused by the decline of effective stress under different weakening degrees. The weakening degree of 30% shows a larger permeability ratio than 20% and 10%, due to the more significant effect of effective stress. However, the larger reservoir permeability will cause more CO_2 injection, and then matrix swelling becomes the dominant factor of permeability changes within Zone 2—indicating that the permeability ratios decreases slightly from the stiffness weakening degree of 10% to 20%, and then 30%. The same phenomenon also occurs at the reference point P2. By the 4000th day, the minimum permeability ratios of stiffness weakening degree from 10% to 30% at this point is 0.61, 0.63, and 0.66, respectively (Figure 21(b)). For Zone 3, reservoir permeability is controlled by two opposing effects—increased effective stress caused by CH_4 pressure deletion and matrix shrinkage induced by CH_4 desorption—due to no CO_2 arrival at this moment. The ultimate permeability distributions within the entire reservoir show a trend alike with Zone 1, indicating the higher stiffness weakening degree caused by CO_2 adsorption, the larger permeability ratio reached (Figure 22). Therefore, neglecting the weakening effect of CO_2 adsorption on coal seam stiffness will underestimate the injection capacity of CO_2.

4.4. Effect of Injection Temperature on CO_2-ECBM.
Gas desorption consumes energy, causing a dropping in reservoir temperature; conversely, gas adsorption would release energy and then elevate the reservoir temperature. For the project of

injection temperature in CO_2-ECBM, the evolution of reservoir temperature is the competitive result of binary gases adsorption/desorption and injected thermal field. However, due to the large volume of coal seam, the migration rate of the apparent temperature rise frond is restricted, resulting in a limited extend of this elevated temperature zone. Taking a case of injection temperature at 320 K, near injection well, reservoir temperature sharply decreases due to the large amount of CH_4 desorption caused by hot CO_2 injection. With the injection continued, reservoir temperature gradually propagates within coal reservoirs, and then it is elevated, while the temperature around production well is lowest due to the net CH_4 desorption caused by reservoir pressure depletion (Figure 23).

With the increasing of injection temperature, both CH_4 production rate and CO_2 storage rate are elevated. The peak production rates for injection at 320, 340, 360, and 380 K are 358.0, 367.8, 375.1, and 380.5 m^3/day, respectively (Figure 24(a)). The corresponding peak CO_2 storage rates are 716.7, 740.7, 760.5, and 775.8 m^3/day, respectively (Figure 24(b))—indicating that higher injection temperature is favorable for CH_4 production and CO_2 storage. At 4000 days, the cumulative CH_4 production and CO_2 storage for no temperature injection are 1.11 and 2.25 million m^3. The cumulative CH_4 production for injection at 320, 340, 360, and 380 K is increased by 1.8% (1.13×10^6 m^3), 3.6% (1.15×10^6 m^3), 4.5% (1.16×10^6 m^3), and 5.4% (1.17×10^6 m^3), respectively (Figure 25(a)). The corresponding CO_2 cumulative storage is increased by 3.1% (2.32×10^6 m^3), 5.3% (2.37×10^6 m^3), 7.1% (2.41×10^6 m^3), and 8.4% (2.44×10^6 m^3), respectively—illustrating that the effect of injection thermal on ECBM production and CO_2 sequestration is gradually moderate with the increase of temperature (Figure 25(b)). Therefore, there is a tradeoff between incremental production/storage and the cost of injection heat. Furthermore, compared with ECBM production, injection temperature is more favorable for CO_2 storage (8.4% versus 5.4% at 4000th day shown in Figure 26).

The mechanism of enhanced CBM recovery and CO_2 sequestration using temperature injection method can be attributed to injection thermal effects on gas adsorption, and thus the permeability evolution. Near the injection well, there is a region (Zone 1 in Figure 27), we defined the thermal dominant area. In this region, matrix swelling induced by CO_2 adsorption is eliminated in some degree due to the raising of reservoir temperature. In addition, higher temperature results in a large amount of CH_4 desorption and then significant matrix shrinkage. The absolute permeability around the injection well is improved by these factors, compared with the case of no injection. However, remote from the injection well (Zone 2 in Figure 27), the effects of thermal on permeability disappear due to the rapid reduction in thermal gradient—showing that lower temperature injection results in a greater permeability. Note that, although the improvement of permeability is slight, it is important for CO_2 injection and CO_2-CH_4 displacement (Figure 28). The effect of coal mass thermal expansion on permeability is not obvious due to the lower magnitude of thermal expansion coefficient (2.4×10^{-5} 1/K).
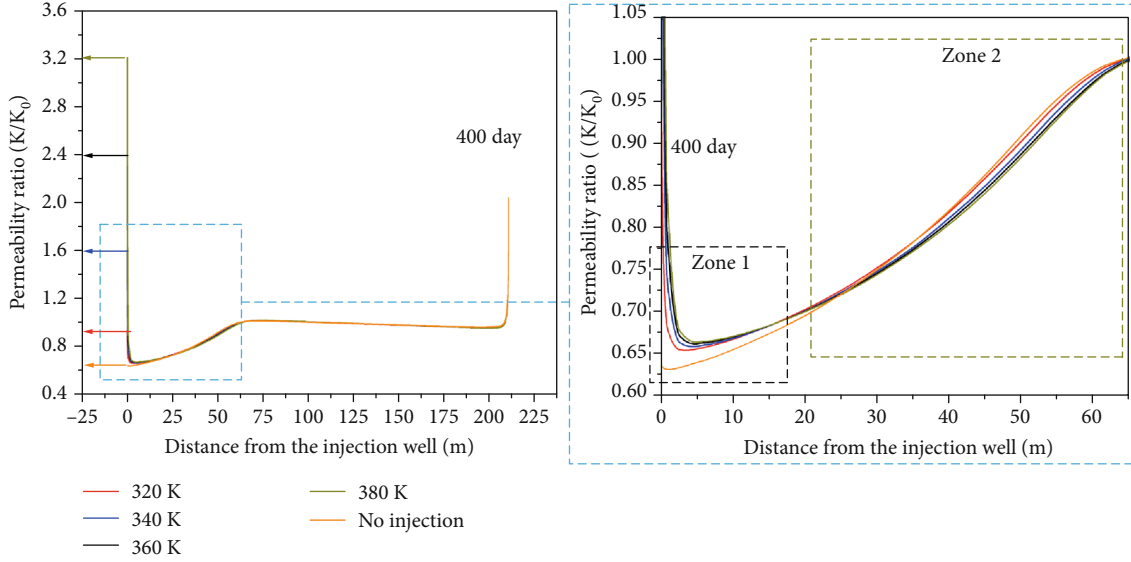
FIGURE 27: Evolution of permeability ratio along reference section A-B.

5. Discussion

With the analysis of "Effect of Coal Stiffness on ECBM," within the coal seam with weak stress sensitivity, the injection of hot CO_2 can moderate a high-stress zone created by matrix swelling near to the injection well and then improve the permeability to achieve more significant production and storage effect.

In the process of CBM recovery, the reservoir pressure continues to decrease and the permeability will increase significantly, which is mainly due to the influence of matrix shrinkage. However, CO_2 sequestration and CO_2-ECBM in deep coal seams usually face the problem of matrix swelling caused by CO_2 adsorption. It is generally recognized that CO_2 injection would be hindered by permeability loss due to the higher adsorption-induced coal matrix swelling in most field-scale pilots, which has also become one of the major obstacles to the implementation of the technology. But it is found in Alberta field trials, opposite to the case of reduction in CO_2 injection rate—CO_2 injectivity was even greater than for weakly adsorbing N_2. This is attributed to the result of coal weakening [39], while noting that the impact has not been quantified. The increase of CO_2 injection rate has also been encountered in other field trials; for instance, the Allison CO_2-ECBM pilot shows the reduction in injection rate during early times, and then the rebound in injectivity during later time. Nevertheless, the rebound in injectivity is believed to be due to the overall reservoir pressure reduction and resulting matrix shrinkage around injection wells instead of coal weakening. Three schemes are designed to investigate the effect of coal weakening on CO_2 injection as shown in Table 6. With the decrease of elastic modulus from 3 to 2.1 GPa (scenario 1), CO_2 injection rate is gradually reduced due to significant matrix swelling during the whole CO_2-ECBM. With the minimum elastic modulus reaching to 1.4 GPa (scenario 2), CO_2 injection rate first
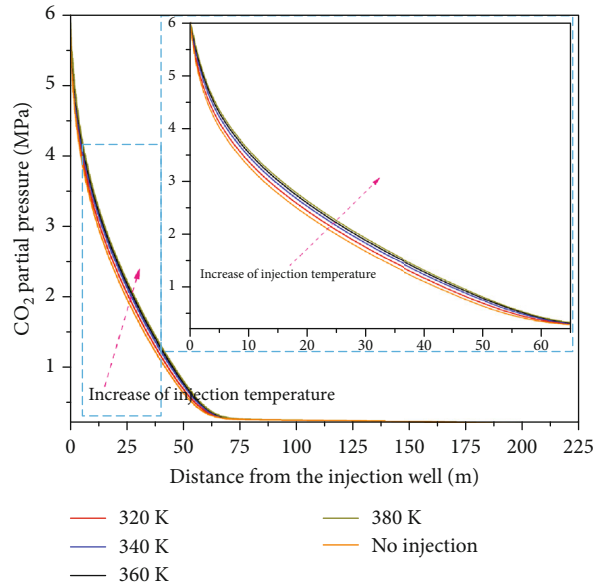
FIGURE 28: Distribution of CO_2 pressure along the section A-B.

TABLE 6: The schemes of investigation on the effect of coal weakening on CO_2 injection.

Schemes	E_{int} (GPa)	ΔE_{max} (GPa)	P_E (MPa)
Scenario 1		1.1	
Scenario 2	3.0	2.0	1.5
Scenario 3		2.5	

decreases and then rebounds slightly during later times. In the case of elastic modulus decreased by 67% from 3 to 1 GPa (scenario 3), CO_2 injection rate shows a trend of slightly decreasing first and then rising sharply due to the

FIGURE 29: The relationship between injection capacity of CO_2 and reduction in elastic modulus. (a) Injection capacity of CO_2. (b) Reduction in elastic modulus.

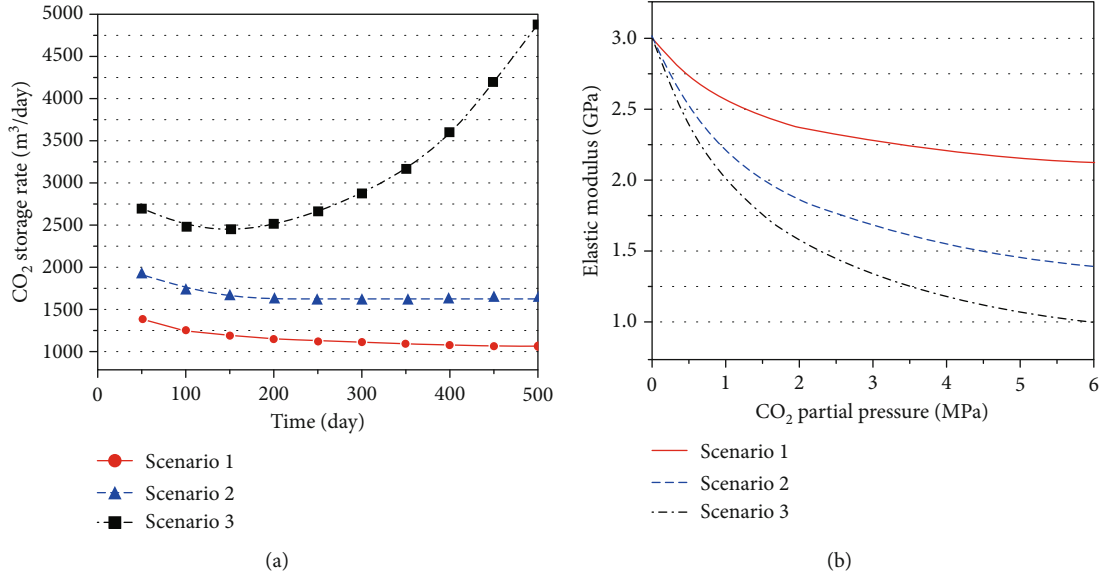TABLE 7: Parameters used to the original R-C model.

Parameters	Value
Coal rank	Subbituminous coal
Initial fracture compressibility (c_0, MPa^{-1})	0.168
Fracture compressibility change rate (α, MPa^{-1})	0.359
Initial porosity (φ_0)	1.5
Poisson's ratio (v)	0.339
Young's modulus (E)	2713
Langmuir strain constant of CO_2 (s_L)	0.03527
Langmuir pressure constant of CO_2 (p_{SL}, MPa)	3.82
Langmuir strain constant of CH_4 (s_L)	0.00931
Langmuir pressure constant of CH_4 (p_{SL}, MPa)	6.1
Langmuir strain constant of N_2 (s_L)	0.00305
Langmuir pressure constant of N_2 (p_{SL}, MPa)	7.72

more pronounced effect of effective stress than matrix swelling (Figure 29). All these discussed above illustrate that the rebound in CO_2 injection rate can be partially attributed to coal weakening, when the elastic modulus decreases by more than 50%.

Interestingly, it is confirmed by many laboratory experiments that CO_2 injection will reduce permeability dramatically. However, the opposite phenomenon is yet shown in some laboratory experiments, with similar to the result of the Alberta field trial. For instance, Robertson and Christiansen [59] describe a new permeability equation derived for sorption-elastic media such as coal specifically for confining conditions found commonly in the laboratory, but not in the field. This model can especially useful when dealing with laboratory experiments where many of the other factors that

cloud field measurements are eliminated. The model can be expressed as follows:

$$
\frac{k}{k_0} = \exp \left[3c_0 \frac{1 - \exp(\alpha \Delta p)}{-\alpha} + \frac{9}{\varphi_0} \frac{(1 - 2v)}{E} \Delta p \\
- \frac{9}{\varphi_0} \frac{s_L p_{SL}}{(p_{SL} + P_0)} \ln \left(\frac{p_{SL} + p}{p_{SL} + P_0} \right) \right],
\tag{43}
$$

where c_0 is the initial cleat compressibility, α is the cleat compressibility change rate, Δp is the change of cleat gas pressure, φ_0 is the initial porosity of the cleat, v is Poisson's ratio, E is the elastic modulus, s_L and p_{SL} are sorption-induced Langmuir strain, and p_0 and p are cleat pressure at initial and current state, respectively.

The Robertson-Christiansen permeability model (R-C model) shown in Eq. (43) was applied to coal permeability data measured in the laboratory under hydrostatic confinement pressure. The permeability data was taken from Robertson and Christiansen [40], and the main parameters are listed in Table 7. The proposed model shows a good match with the measured data from N_2 (Figure 30(a)). CH_4 had a larger sorption strain value than did N_2. Permeability ratios first decrease due to matrix swelling caused by CH_4 adsorption and then rebounds due to the decline of effective stress. However, the prediction value of the R-C model underestimated the actual permeability (Figure 30(b)). Robertson and Christiansen [40] attribute the poor fit of permeability data to the difference between stress-free sorption-induced strain and constrained sorption-induced strain—the amount of sorption-induced strain measured under confining stress condition will be significantly less than that measured under unconfined state (stress-free). Therefore, freestanding sorption-induced strain could be used into the permeability model due to easily accessible, but it should be modified
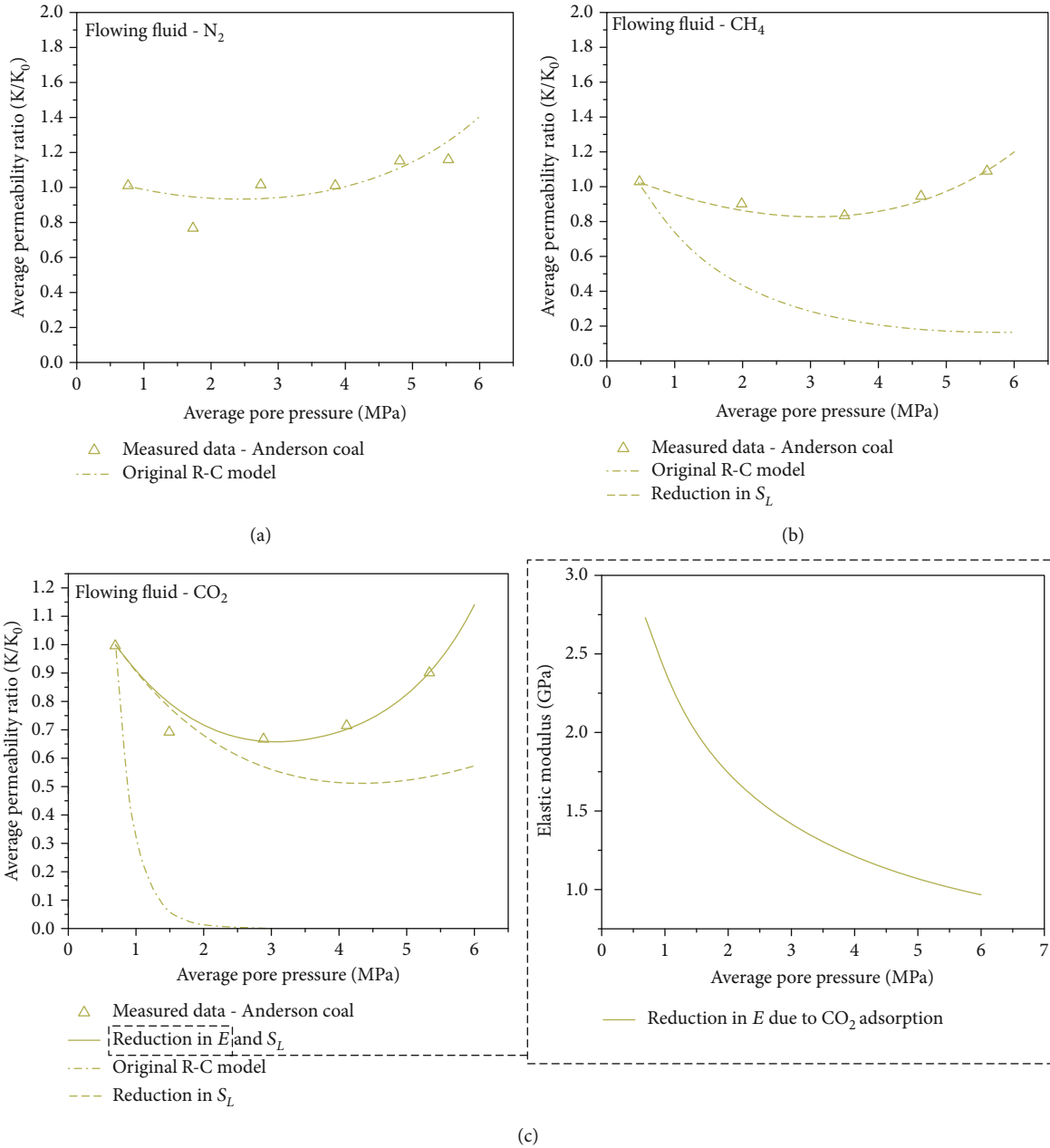
(a)

(b)

(c)

FIGURE 30: Permeability evolution under different flowing fluid (data from [40]).

before being inputted into the model to account for the depression of sorption-induced strain caused by partially confined matrix blocks. Here, we can try to correct the effect of this discrepancy by decreasing the input parameter of sorption-induced strain from 0.00931 to 0.00325, and then the result shows that the modified model matched the measured data for CH_4 very well (Figure 30(b)). Though, the adsorption of CO_2 has a much larger sorption-induced strain (0.03527) than CH_4 (0.00931) and N_2 (0.00305). When CO_2 is a flowing fluid, the actual permeability ratio is still vastly underestimated by the prediction model (Figure 30(c)). The model is modified by sharply reducing the CO_2 sorption-induced strain from 0.03527 to 0.00437, while there is still a larger difference between the theoretical value and the actual. Thus, considering the effect of CO_2 adsorption on coal

mechanics—reduction in elastic modulus—we update the R-C model again, and then the predictions of this modified model are in perfect agreement with the permeability data from CO_2. With the increase of CO_2 pressure from 0.7 to 5.32 MPa, the elastic modulus of this perfect model decreases by 63% from 2.7 to 1 GPa, illustrating that the effect of matrix swelling on permeability variation may be not pronounced compared to the decreasing effective stress under high confining pressure.

CO_2 sequestration and CO_2-ECBM projects are preferred to be carried out in deep unminable coal seams where supercritical CO_2 is most likely to be encountered due to a high enough *in situ* stress and temperature. In this case, care should be considered that CO_2 interaction induced significant mechanical characteristics alterations and then changed

permeability in coal. Therefore, it is necessary to further investigate the influence of CO_2 adsorption on coal mechanics under constrained adsorption state.

6. Conclusion

(1) Injection of CO_2/N_2 all can reach the purpose of ECBM, while the significant coal matrix swelling induced by CO_2 adsorption can reduce the reservoir permeability by one order of magnitude at least, and thus, it is not conducive to continuous CO_2 injection and ECBM. The effect of N_2-ECBM overmatches CO_2 injection. However, the net matrix shrinkage could cause a sharply increase of permeability and then early N_2 breakthrough

(2) The elastic modulus of coal seam affects reservoir permeability by controlling the stiffness of the coal cleat system. Harder coal seam is beneficial to the primary production due to the larger permeability recovery. On the contrary, for the CO_2/N_2 injection project, softer coal seam results in greater ECBM production and CO_2 sequestration. Compared to primary CBM recovery and CO_2-ECBM, N_2-ECBM is more sensitive to the stiffness of coal seam

(3) CO_2 adsorption not only induces matrix swelling but also accompanies the reductions in stiffness of coal seam and then shows a significant effect on permeability changes and CO_2 storage. With approaching the injection well, reservoir permeability for different CO_2 weakening degree presents the distribution of "S" type, showing that permeability evolution is dominated by decreasing of effective stress around injection well and then controlled by matrix swelling remote from injection well. With the increase of the weakening degree of coal seam stiffness, CO_2 cumulative storage shows an increasing trend. Neglecting the weakening effect of CO_2 adsorption on coal seam stiffness will underestimate the injection capacity of CO_2

(4) Injection of hot CO_2 could improve the permeability around injection well and then enhance CO_2 cumulative storage and CBM recovery. The effect of injection thermal on ECBM production and CO_2 sequestration is gradually moderate with the increase of temperature. Furthermore, compared with ECBM production, injection temperature is more favorable for CO_2 storage, especially within hard coal seams.

Data Availability

The data used to support the findings of this study are available from the first author upon request.

Conflicts of Interest

The authors declare no conflict of interest.

Authors' Contributions

Hao Han and Shun Liang conceived and designed the numerical simulation scheme. Hao Han, Yaowu Liang, Chuanjin Tang, and Liqiang Yu performed the numerical simulation software. Yaowu Liang and Chuanjin Tang helped Hao Han analyze the data. JunQiang Kang and Liqiang Yu supported the research in terms of both scientific and technical expertise. Hao Han and Yaowu Liang wrote the original draft. Shun Liang and Xuehai Fu revised the manuscript.

Acknowledgments

References

[1] Q. Ma, S. Harpalani, and S. Liu, "A simplified permeability model for coalbed methane reservoirs based on matchstick strain and constant volume theory," *International Journal of Coal Geology*, vol. 85, no. 1, pp. 43–48, 2011.

[2] J.-Q. Shi and S. Durucan, "Exponential growth in san Juan Basin Fruitland coalbed permeability with reservoir Drawdown: model match and new Insights," *SPE Reservoir Evaluation & Engineering*, vol. 13, no. 6, pp. 914–925, 2010.

[3] S. Zhang, J. Liu, M. Wei, and D. Elsworth, "Coal permeability maps under the influence of multiple coupled process," *International Journal of Coal Geology*, vol. 187, pp. 71–82, 2018.

[4] K. H. S. M. Sampath, M. S. A. Perera, P. G. Ranjith et al., "CH_4-CO_2 gas exchange and supercritical CO_2 based hydraulic fracturing as CBM production-accelerating techniques: a review," *Journal of Carbon Dioxide Utilization*, vol. 22, pp. 212–230, 2017.

[5] S. Tao, S. Chen, and Z. Pan, "Current status, challenges, and policy suggestions for coalbed methane industry development in China: a review," *Energy Science & Engineering*, vol. 7, no. 4, pp. 1059–1074, 2019.

[6] S. Tao, Z. Pan, S. Tang, and S. Chen, "Current status and geological conditions for the applicability of CBM drilling technologies in China: a review," *International Journal of Coal Geology*, vol. 202, pp. 95–108, 2019.

[7] S. Ottiger, R. Pini, G. Storti, and M. Mazzotti, "Measuring and modeling the competitive adsorption of CO2, CH4, and N2 on a dry coal," *Langmuir*, vol. 24, no. 17, pp. 9531–9540, 2008.

[8] J. Lin, T. Ren, G. Wang, and J. Nemcik, "Simulation investigation of N_2 injection enhanced gas drainage: model development and identification of critical parameters," *Journal of Natural Gas Science and Engineering*, vol. 55, pp. 30–41, 2018.

[9] R. E. Rogers and R. Rogers, *Coalbed methane: principles and practice*, PTR Prentice Hall, Englewood Cliffs, NJ, USA, 1994.

[10] M. Mukherjee and S. Misra, "A review of experimental research on enhanced coal bed methane (ECBM) recovery via CO_2 sequestration," *Earth Science Reviews*, vol. 179, pp. 392–410, 2018.

[11] J.-Q. Shi and S. Durucan, "A model for changes in coalbed permeability during primary and enhanced methane recovery," *SPE Reservoir Evaluation & Engineering*, vol. 8, no. 4, pp. 291–299, 2005.

[12] Y. Fan, C. Deng, X. Zhang, F. Li, X. Wang, and L. Qiao, "Numerical study of CO_2-ehanced coalbed methane recovery," *International Journal of Greenhouse Gas Control*, vol. 76, pp. 12–23, 2018.

[13] S. Durucan and J. Shi, "Improving the CO_2 well injectivity and enhanced coalbed methane production performance in coal seams," *International Journal of Coal Geology*, vol. 77, pp. 214–221, 2008.

[14] W. D. Gunter, M. J. Mavor, and J. R. Robinson, "CO_2 storage and enhanced methane production: field testing at Fenn-Big Valley, Alberta, Canada, with application," in *Proceedings of the 7th International Conference on Greenhouse Gas Control Technologies (GHGT-7)*, pp. 413–421, Vancouver, Canada, 2005.

[15] D. Y. C. Leung, G. Caramanna, and M. M. Maroto-Valer, "An overview of current status of carbon dioxide capture and storage technologies," *Renewable and Sustainable Energy Reviews*, vol. 39, pp. 426–443, 2014.

[16] Y. Wu, J. Liu, Z. Chen, D. Elsworth, and D. Pone, "A dual poroelastic model for CO_2-enhanced coalbed methane recovery," *International Journal of Coal Geology*, vol. 86, no. 2-3, pp. 177–189, 2011.

[17] Z. Pan and L. D. Connell, "Modelling permeability for coal reservoirs: a review of analytical models and testing data," *International Journal of Coal Geology*, vol. 92, pp. 1–44, 2012.

[18] J. Shi and S. Durucan, "Modelling laboratory horizontal stress and coal permeability data using S&D permeability model," *International Journal of Coal Geology*, vol. 131, pp. 172–176, 2014.

[19] L. D. Connell, M. Lu, and Z. J. Pan, "An analytical coal permeability model for tri-axial strain and stress conditions," *International Journal of Coal Geology*, vol. 84, no. 2, pp. 103–114, 2010.

[20] L. D. Connell, "A new interpretation of the response of coal permeability to changes in pore pressure, stress and matrix shrinkage," *International Journal of Coal Geology*, vol. 162, pp. 169–182, 2016.

[21] H. Kumar, D. Elsworth, J. P. Mathews, J. Liu, and D. Pone, "Effect of CO_2 injection on heterogeneously permeable coalbed reservoirs," *Fuel*, vol. 135, pp. 509–521, 2014.

[22] X. Cui and R. M. Bustin, "Volumetric strain associated with methane desorption and its impact on coalbed gas production from deep coal seams," *AAPG Bulletin*, vol. 89, no. 9, pp. 1181–1202, 2005.

[23] J. Q. Shi and S. Durucan, "A numerical simulation study of the Allison Unit CO_2-ECBM pilot: the impact of matrix shrinkage and swelling on ECBM production and CO_2 injectivity," in *Greenhouse Gas Control Technologies (GHGT7)*, Peer Reviewed Papers and Overviews, E. S. Rubin, D. W. Keith, and C. F. Gilboy, Eds., pp. 431–439, Elsevier, 2005.

[24] M. Fujioka, M. Yamaguchi, and M. Nako, "CO_2-ECBM field tests in the Ishikari Coal Basin of Japan," *International Journal of Coal Geology*, vol. 82, no. 3-4, pp. 287–298, 2010.

[25] M. Hadi Mosleh, M. Sedighi, P. J. Vardon, and M. Turner, "Efficiency of carbon dioxide storage and enhanced methane recovery in a high rank coal," *Energy & Fuels*, vol. 31, no. 12, pp. 13892–13900, 2017.

[26] K. H. S. M. Sampath, M. S. A. Perera, P. G. Ranjith, and S. K. Matthai, "CO_2 interaction induced mechanical characteristics alterations in coal: a review," *International Journal of Coal Geology*, vol. 204, pp. 113–129, 2019.

[27] M. S. Masoudian, D. W. Airey, and A. El-Zein, "Experimental investigations on the effect of CO_2 on mechanical of coal," *International Journal of Coal Geology*, vol. 128, pp. 12–23, 2014.

[28] M. Meng and Z. Qiu, "Experiment study of mechanical properties and microstructures of bituminous coals influenced by supercritical carbon dioxide," *Fuel*, vol. 219, pp. 223–238, 2018.

[29] M. A. Pirzada, M. Zoorabadi, H. Lamei Ramandi, I. Canbulat, and H. Roshan, "CO_2 sorption induced damage in coals in unconfined and confined stress states: a micrometer to core scale investigation," *International Journal of Coal Geology*, vol. 198, pp. 167–176, 2018.

[30] X. Zhang, P. G. Ranjith, A. S. Ranathunga, and D. Li, "Variation of mechanical properties of bituminous coal under CO_2 and H_2O saturation," *Journal of Natural Gas Science and Engineering*, vol. 61, pp. 158–168, 2018.

[31] V. Vishal, P. G. Ranjith, and T. N. Singh, "An experimental investigation on behaviour of coal under fluid saturation, using acoustic emission," *Journal of Natural Gas Science and Engineering*, vol. 22, pp. 428–436, 2015.

[32] A. S. Ranathunga, M. S. A. Perera, P. G. Ranjith, and R. H. Bui, "Super-critical CO_2 saturation-induced mechanical property alterations in low rank coal: an experimental study," *Journal of Supercritical Fluids*, vol. 109, pp. 134–140, 2016.

[33] M. S. A. Perera, P. G. Ranjith, and D. R. Viete, "Effects of gaseous and super-critical carbon dioxide saturation on the mechanical properties of bituminous coal from the Southern Sydney Basin," *Applied Energy*, vol. 110, pp. 73–81, 2013.

[34] X. Zhang, P. G. Ranjith, Y. Lu, and A. S. Ranathunga, "Experimental investigation of the influence of CO_2 and water adsorption on mechanics of coal under confining pressure," *International Journal of Coal Geology*, vol. 209, pp. 117–129, 2019.

[35] B. Gathitu, W. Chen, and M. McClure, "Effects of coal interaction with supercritical CO_2: physical structure," *Industrial and Engineering Chemistry Research*, vol. 48, no. 10, pp. 5024–5034, 2009.

[36] Y. Zhang, M. Lebedev, M. Sarmadivaleh, A. Barifcani, and S. Iglauer, "Swelling-induced changes in coal microstructure due to supercritical CO_2 injection," *Geophysical Research Letters*, vol. 43, no. 17, pp. 9077–9083, 2016.

[37] H. Guo, X. Ni, Y. Wang, X. Du, T. Yu, and R. Feng, "Experimental study of CO_2-watermineral interactions and their influence on the permeability of coking coal and implications for CO_2-ECBM," *Minerals*, vol. 8, no. 3, pp. 117–138, 2018.

[38] S. Farquhar, J. Pearce, G. Dawson et al., "A fresh approach to investigating CO_2 storage: experimental CO_2-water-rock interactions in a low- salinity reservoir system," *Chemical Geology*, vol. 399, pp. 98–122, 2015.

[39] M. J. Mavor, W. D. Gunter, and J. R. Robinson, "Alberta Multiwell Micro-pilot testing for CBM properties, enhanced methane recovery and CO_2 storage potential," in *SPE Annual*

Technical Conference and Exhibition, pp. 26–29, Houston, Texas, 2004.

[40] E. P. Robertson and R. L. Christiansen, "Modeling laboratory permeability in coal using sorption-induced strain data," *SPE Reservoir Evaluation and Engineering*, vol. 10, pp. 260–269, 2013.

[41] W. Zhu, C. Wei, J. Liu, H. Qu, and D. Elsworth, "A model of coal-gas interaction under variable temperatures," *International Journal of Coal Geology*, vol. 86, no. 2-3, pp. 213–221, 2011.

[42] C. Fan, D. Elsworth, S. Li, L. Zhou, Z. Yang, and Y. Song, "Thermo-hydro-mechanical-chemical couplings controlling CH_4 production and CO_2 sequestration in enhanced coalbed methane recovery," *Energy*, vol. 173, pp. 1054–1077, 2019.

[43] C. Fan, D. Elsworth, S. Li et al., "Modelling and optimization of enhanced coalbed methane recovery using CO_2/N_2 mixtures," *Fuel*, vol. 253, pp. 1114–1129, 2019.

[44] S. Liang, H. Han, D. Elsworth et al., "Evolution of production and transport characteristics of steeply-dipping ultra-thick coalbed methane reservoirs," *Energies*, vol. 13, no. 19, p. 5081, 2020.

[45] Q. Liu, Y. Cheng, H. Wang et al., "Numerical assessment of the effect of equilibration time on coal permeability evolution characteristics," *Fuel*, vol. 140, pp. 81–89, 2015.

[46] F. An, Y. Cheng, L. Wang, and W. Li, "A numerical model for outburst including the effect of adsorbed gas on coal deformation and mechanical properties," *Computers and Geotechnics*, vol. 54, pp. 222–231, 2013.

[47] A. S. Ziarani, R. Aguilera, and C. R. Clarkson, "Investigating the effect of sorption time on coalbed methane recovery through numerical simulation," *Fuel*, vol. 90, no. 7, pp. 2428–2444, 2011.

[48] J. Liu, Z. Chen, D. Elsworth, H. Qu, and D. Chen, "Interactions of multiple processes during CBM extraction: a critical review," *International Journal of Coal Geology*, vol. 87, no. 3-4, pp. 175–189, 2011.

[49] T. Teng, Y. Zhao, F. Gao, J. G. Wang, and W. Wang, "A fully coupled thermo-hydro-mechanical model for heat and gas transfer in thermal stimulation enhanced coal seam gas recovery," *International Journal of Heat and Mass Transfer*, vol. 125, pp. 866–875, 2018.

[50] F. Tong, L. Jing, and R. W. Zimmerman, "A fully coupled thermo-hydro-mechanical model for simulating multiphase flow, deformation and heat transfer in buffer material and rock masses," *International Journal of Rock Mechanics and Mining Sciences*, vol. 47, no. 2, pp. 205–217, 2010.

[51] H. Qu, J. Liu, Z. Chen et al., "Complex evolution of coal permeability during CO_2 injection under variable temperatures," *International Journal of Greenhouse Gas Control*, vol. 9, pp. 281–293, 2012.

[52] Y. Mu, Y. Fan, J. Wang, and N. Fan, "Numerical study on injection of flue gas as a heat carrier into coal reservoir to enhance CBM recovery," *Journal of Natural Gas Science and Engineering*, vol. 72, p. 103017, 2019.

[53] X. Su, X. Lin, S. Liu, M. Zhao, and Y. Song, "Geology of coalbed methane reservoirs in the Southeast Qinshui Basin of China," *International Journal of Coal Geology*, vol. 64, pp. 197–210, 2005.

[54] Z. Pan, J. Ye, F. Zhou, Y. Tan, L. D. Connell, and J. Fan, "CO_2 storage in coal to enhance coalbed methane recovery: a review

of field experiments in China," *International Geology Review*, vol. 60, no. 5-6, pp. 754–776, 2018.

[55] S. Wong, D. Law, X. Deng et al., "Enhanced coalbed methane and CO_2 storage in anthracitic coals–micro-pilot test at South Qinshui, Shanxi, China," *International Journal of Greenhouse Gas Control*, vol. 1, no. 2, pp. 215–222, 2007.

[56] X. Sun, Y. Zhang, K. Li, and Z. Gai, "A new mathematical simulation model for gas injection enhanced coalbed methane recovery," *Fuel*, vol. 183, pp. 478–488, 2016.

[57] M. S. Masoudian, "Multiphysics of carbon dioxide sequestration in coalbeds: a review with a focus on geomechanical characteristics of coal," *Journal of Rock Mechanics and Geotechnical Engineering*, vol. 8, no. 1, pp. 93–112, 2016.

[58] M. S. Masoudian, D. W. Airey, and A. El-Zein, "The role of coal seam properties on coupled processes during CO_2 sequestration: a parametric study," *Greenhouse Gases: Science and Technology*, vol. 4, pp. 492–518, 2016.

[59] E. P. Robertson and R. L. Christiansen, "A permeability model for coal and other fractured, Sorptive-Elastic Media," *SPE Journal*, vol. 13, pp. 314–324, 2006.